



Scale-wise coherent vorticity extraction for conditional statistical modeling of homogeneous isotropic two-dimensional turbulence

Romain Nguyen van yen^{a,*}, Marie Farge^a, Kai Schneider^b

^a LMD-CNRS-IPSL, École Normale Supérieure, 24 rue Lhomond, 75231 Paris cedex 5, France

^b M2P2-CNRS and CMI, Université d'Aix-Marseille, 39 rue Joliot-Curie, 13453 Marseille cedex 13, France

ARTICLE INFO

Article history:
Available online 6 June 2011

Keywords:
Turbulence
Wavelets
Coherent vorticity extraction
Maximum entropy

ABSTRACT

Classical statistical theories of turbulence have shown their limitations, in that they cannot predict much more than the energy spectrum in an idealized setting of statistical homogeneity and stationarity. We explore the applicability of a conditional statistical modeling approach: can we sort out what part of the information should be kept, and what part should be modeled statistically, or, in other words, “dissipated”? Our mathematical framework is the initial value problem for the two-dimensional (2D) Euler equations, which we approximate numerically by solving the 2D Navier–Stokes equations in the vanishing viscosity limit. In order to obtain a good approximation of the inviscid dynamics, we use a spectral method and a resolution going up to 8192^2 . We introduce a macroscopic concept of dissipation, relying on a split of the flow between coherent and incoherent contributions: the coherent flow is constructed from the large wavelet coefficients of the vorticity field, and the incoherent flow from the small ones. In previous work, a unique threshold was applied to all wavelet coefficients, while here we also consider the effect of a scale by scale thresholding algorithm, called scale-wise coherent vorticity extraction. We study the statistical properties of the coherent and incoherent vorticity fields, and the transfers of enstrophy between them, and then use these results to propose, within a maximum entropy framework, a simple model for the incoherent vorticity. In the framework of this model, we show that the flow velocity can be predicted accurately in the L^2 norm for about 10 eddy turnover times.

© 2011 Elsevier B.V. All rights reserved.

1. Introduction

Fluid flows are said to be in the fully developed turbulent regime when they are highly disordered and dominated by nonlinear effects due to inertia, which occurs when their Reynolds number, Re , is large. Competing tendencies to form and to dislocate coherent structures then create motion over a wide range of spatial and temporal scales. In the special case of periodic two-dimensional (2D) decaying turbulence, on which we focus in this paper, merging processes tend to win the game and the average size of structures increases. Kraichnan has shown that this basic phenomenology could be understood with the help of a dual cascade paradigm, in which enstrophy and energy are sent respectively towards scales finer and coarser than the integral scale of the flow ([1], hereafter K67). Within the simplified setting in which energy and enstrophy are injected around a characteristic wavenumber k_l , he established that the enstrophy cascade would occur between k_l and a cut-off wavenumber $k_D \propto$

$Re^{1/2}$, and that for large Re the energy spectrum would become Re independent and approach the universal scaling $E(k) \propto k^{-3}$. Such an energy spectrum is associated to a k -independent enstrophy flux from small wavenumber modes to large wavenumber modes. The range of k between k_l and k_D is called the inertial range, while wavenumbers k larger than k_D constitute the molecular dissipation range. The relevance of the enstrophy cascade for the phenomenological description of decaying 2D turbulence is supported by numerical experiments [2,3].

The K67 theory is completely statistical, in the sense that it does not claim to predict anything about the time evolution of a flow, but invokes only generic features of all turbulent flows satisfying certain hypotheses, that is, of all elements of a large ensemble. It may be criticized on the grounds that realistic flows, such as a jet or the wake behind an obstacle, typically do not satisfy its underlying assumptions. Even in the restricted setting where the theory is approximately valid, one may be interested in the history of the flow and not only in properties of a global attractor. Another shortcoming of the K67 theory is that it is inconsistent with a mathematical theorem. Indeed, one of its essential hypotheses is that the enstrophy dissipation rate does not go to zero in the limit $Re \rightarrow \infty$. But it is well known [4] that, in the limit $Re \rightarrow \infty$, smooth solutions of the 2D Navier–Stokes

* Corresponding author.
E-mail addresses: rnguyen@lmd.ens.fr (R. Nguyen van yen), farge@lmd.ens.fr (M. Farge).

equations (NSE) with smooth forcing converge in the enstrophy norm to smooth solutions of the 2D Euler equations (corresponding to $Re = \infty$), which have constant enstrophy. This paradox, which had already been predicted using a closure model [5], and pointed out in [6], was recently revisited by high resolution direct numerical simulation (DNS) of the 2D NSE [7,8]. It was shown that even though the enstrophy dissipation rate is bounded by $C(t)Re^{-1}$ when $Re \rightarrow \infty$ (a mathematical theorem!), the decay with Re that can be observed in practice is only logarithmic, because $C(t)$ increases extremely quickly. The implications of this result on the statistical theory of 2D turbulence were recently outlined in [9] (see also [10] for a different viewpoint). It was argued that no Reynolds-independent quantity was available to characterize dissipation, and that the hope of a Reynolds-independent description of 2D turbulence had to be given up.

This conclusion is somewhat disappointing, given the already mentioned convergence of smooth solutions to the 2D Navier–Stokes equations in a periodic domain towards solutions to the 2D Euler equations [4]. Convergence occurs at a relatively fast rate $O(Re^{-1})$ in the energy norm, so that Re -dependent effects can be seen as perturbations on top of the inviscid behavior. In the presence of walls imposing no-slip boundary conditions, the 2D Euler equations are also well posed, but their solutions behave very differently from those of the Navier–Stokes solutions even at large Re , and the problem is much more delicate; see, e.g., [11] for a discussion. The 3D case also presents formidable difficulties. But in the 2D wall-less case, on which we focus in this paper, the initial value problem for the incompressible Euler equations is a solid foundation from which features of 2D turbulence should be deduced. In fact, the use of inviscid equations, sometimes along with an ad hoc regularization mechanism, is widespread in numerical models, for example in geophysical fluid dynamics [12]. Hence the main obstacle may lie in our inability to ask the right questions.

In the search for a reduced description of hydrodynamic turbulence, the detailed study of reference solutions obtained from well validated numerical methods remains an important ingredient. Therefore, although our long term goal is to build a reduced description of 2D turbulence based on the wavelet representation, we limit ourselves in the present contribution to the analysis of fully developed decaying 2D turbulent flows starting from first principles. From this a priori analysis, we are able to study several wavelet-based models and to establish their essential features. We hope that the resulting picture of 2D turbulence will provide a way towards more predictive approaches.

In the first section, we recall the general notion of incomplete statistical equilibrium, and explain how it was studied by Kraichnan and others in the context of turbulence. We then describe the mathematical setting and the numerical tools that we have chosen for our specific study of 2D decaying turbulence. After a brief reminder on wavelet theory, we present a set of results about the statistics of 2D turbulence. We then recall the coherent vorticity extraction procedure, which aims to split the degrees of freedom of a turbulent flow into a noisy part and a deterministic part. Subsequently, we study the transfer of enstrophy between these two parts, both from a Fourier view point and from a wavelet view point. In the last section, we study the retroaction of the noisy vorticity component onto the rest of the flow. Finally, we discuss the overall results and draw some conclusions.

2. Conditional statistical modeling

Predictable quantities in turbulent flows can only be defined in a statistical sense, as was already remarked by Burgers [13] and Taylor [14]. In the 2D case, absolute statistical equilibria assuming only conservation of energy and enstrophy were derived

by Kraichnan [1] and observed numerically by Basdevant and Sadourny [15] after a long time in simulations of the Galerkin truncated 2D Euler equations. Solutions to the full 2D Euler equations never reach these absolute equilibria, due to their lack of truncation at fine scales, which allows enstrophy to escape towards infinitely high wavenumber regions of the spectrum. Instead, these solutions tend to follow the phenomenology associated to the already introduced K67 theory, but no rigorous statistical ensemble has been constructed to explain this observation. In a stationary setting, one may try to derive the K67 theory by studying the invariant measure of the dynamical system associated to the Euler equations (see, e.g., [16] and related papers). But the fact that the same phenomenology can be observed in freely decaying flows suggests that the stationarity hypothesis is superfluous. In any case, as argued by many authors, even a detailed understanding of the invariant measure may yield little useful information about the behavior of a particular solution, because of the slow and non-uniform sampling of the attractor (see, e.g., [17]). However, if one considers a flow that is evolving in time, we already know that it is a solution to the Navier–Stokes equations, which are completely deterministic, and there is no objective way to introduce a statistical ensemble (see [18] for more along this line).

To understand the difficulty, let us first consider the relatively easier case of classical kinetic theory [19]. In the fluid approximation, many-body systems are considered to be in a state of local thermodynamic equilibrium and are described by a few macroscopic fields, such as velocity and temperature. The local Maxwellian distribution of particle velocities can be recovered by maximizing entropy with the constraint that the macroscopic fields take their known value in each point. Therewith the statistical ensemble containing possible realizations of the microscopic degrees of freedom is defined as a direct product of local ensembles corresponding to each fluid particle. As long as the hypothesis of local thermodynamic equilibrium holds, the equations governing the evolution of macroscopic quantities depend on the particular realization of the microscopic motion only through a stochastic forcing term, which is neglected in practice. There is thus a perfect separation between microscopic and macroscopic motions. If one changes, by thought experiment, the sign of the velocity of a single molecule in such a fluid, the microscopic motion soon takes an entirely different trajectory, but there is no measurable influence on the macroscopic velocity field. The only signatures of the microscopic properties of the system are the friction terms in the fluid equations. When energy is transferred to microscopic motion, it is dissipated, or “thrown away” according to the Latin etymology, evocative of an irreversible loss of information.

Now, due to the apparent disorder of the macroscopic velocity field itself, it seems desirable to refine the separation by distinguishing between two classes of macroscopic degrees of freedom, those which we want to predict, and those which are to be replaced by statistical distributions or, in other words, “thrown away” to join their microscopic comrades. Kraichnan [20] gave an intuitive argument in favor of such an intermediate description over a fully statistical one. Comparing the characteristic time needed to spread energy in space within a given scale, and the characteristic time needed to transfer energy between scales, he noted that they were of the same order of magnitude. In other words, active flow elements will not completely forget their location in space before they start getting distorted, and, conversely, will not completely forget their shape before they move to another location in space. These active flow elements may be amenable to a deterministic treatment, while others call for a statistical description. Kraichnan and Chen [21] went further, asserting that “Turbulence [...] is an interplay of order and disorder, associated with strong departure from absolute statistical equilibrium”. They noted that advanced statistical models such

as the direct interaction approximation (DIA) [22] could not faithfully describe the dynamics of very simple dissipative systems. To develop a better description, they proposed the concept of “constrained decimation”, which consists in splitting the degrees of freedom of the flow into two parts:

- those that are modeled statistically, which collectively constitute the “dissipated” flow,
- those whose time evolution is described by an initial value problem, which we call “explicit”, following [21].

To each definition of the explicit flow thus corresponds a notion of dissipation, or transfer of energy (or enstrophy) from explicit to dissipated degrees of freedom. The notion of “degrees of freedom” is used here in a loose sense that will be made more rigorous later on. What is important is that the split is not necessarily static, but can depend on the instantaneous flow, or even on its history. Indeed, this approach, to which we refer as conditional statistical modeling, is time dependent by construction, and in it no assumptions are made about the stationarity of the solution. The same idea was later elaborated by several authors; see the review by Kraichnan [23] and references therein. Due to the nonlinear term, it is likely that, contrary to the microscopic degrees of freedom, the dissipated flow retroacts strongly onto the explicit flow and cannot be neglected or even treated perturbatively. Hence the frontier between the two can a priori be chosen subjectively, but the strength and qualitative properties of the retroaction of the dissipated flow onto the explicit flow determines a posteriori the practical relevance of the split.

In fact, the idea of extending the notion of dissipation to macroscopic degrees of freedom in turbulent flows goes back at least to Richardson and Gaunt [24]. The classes they had in mind can be roughly termed “coarse scale motion” and “fine scale motion”, and therefore the dissipation so defined was formally equivalent to an eddy viscosity, for which Prandtl had given a formula five years earlier [25], and which has remained the dominant paradigm ever since. More advanced methods have also been developed based on the same splitting between coarse and fine scales, for example large eddy simulation (LES) [26] and nonlinear Galerkin [27]. In the last ten years, more advanced statistical physics concepts have been developed in this context [28], and applied for example to describe multiscale atmospheric flows [29] or solutions of dispersive nonlinear wave equations [30]. But from equilibrium statistical physics we know that the correctness of the predictions depends highly on the choice of the right variables to describe the system. It is therefore an important research topic to explore different concepts of dissipation in turbulent flows. The goal of this paper is to explore two alternatives to the coarse scale/fine scale split. They are both based on the wavelet representation of the vorticity field, which has been advocated since the late 1980s as an improvement over the more classical Fourier representation [31–33]. Multiscale expansions can be seen as a natural follow up on the wavenumber band expansions studied by Kraichnan in [20], with the essential improvement of maintaining some space locality in the description. Interestingly, they were also encouraged by Jaynes (see the remarks at the end of [34]).

On the long list of remaining issues, there is the matter of how to choose the statistical model for the dissipated flow. By analogy with the Gibbs entropy of equilibrium statistical mechanics, the entropy S_F of the flow can be defined as the Shannon entropy [35] computed from the statistical distribution of the dissipated degrees of freedom (see Section 7.1). Following the ideas of Jaynes [36], the distribution that should be chosen to make the most unbiased predictions about the future evolution of the flow is the one that maximizes S_F . We should keep in mind that the goal of entropy maximization is to avoid biased results, and not to optimize the predictions of a model. Maximal entropy

predictions are not necessarily good; in fact, they may even be completely worthless if the split between explicit and dissipated degrees of freedom has been ill chosen.

In the following, we want to consider a single solution to the initial value problem for the Euler equation, and see how these ideas fit together to describe it.

3. Mathematical framework and numerical method

In any modeling effort there is, a priori, a phase of analysis, in which information is gathered either from experiments or from a well established underlying model, and, a posteriori, a phase of synthesis, in which the new model is validated. Although our long term goal is to help improve existing statistical models and computational methods, we focus here on the a priori analysis stage, having in mind the word of wisdom of Meneveau and Katz [37]: “a posteriori tests typically do not provide much insight into the detailed physics of models and the reasons that they do or do not work”. Therefore we set out to study numerical solutions to the 2D Navier–Stokes equations, an approach commonly known as direct numerical simulation (DNS), and since we are interested in time-dependent properties of the flow and not only in stationary statistics, we work on the initial value problem:

$$\begin{cases} \partial_t \omega + (\mathbf{u} \cdot \nabla) \omega + \nu (-\Delta)^\alpha \omega = 0 \\ \nabla \cdot \mathbf{u} = 0, \quad \omega = \nabla \times \mathbf{u}, \quad \omega(\cdot, t_0) = \omega_0, \end{cases} \quad (1)$$

where the unknown vorticity $\omega(\mathbf{x}, t)$ is a scalar field defined on $\mathbb{T}^2 \times [t_0, t_1]$, $\mathbb{T}^2 = (\mathbb{R}/\mathbb{Z})^2$ is the unit torus, t_0 and t_1 are respectively the initial and final time, \mathbf{u} is the velocity field, ν is the fluid viscosity, $\alpha \in \mathbb{N}^*$, and ω_0 is a smooth initial vorticity field. Classical results guarantee the existence and uniqueness of a solution $\omega(\mathbf{x}, t)$ to problem (1) in a suitable function space; see [38]. These results extend to the case of the incompressible Euler equations, corresponding to $\nu = 0$ in (1); see [11]. When $\alpha = 1$, the equations given as (1) are called Navier–Stokes equations (NSE), and when $\alpha > 1$ they are called hyperdissipative NSE (HNSE) [39]. Hyperdissipation is an ad hoc regularization mechanism for the incompressible Euler equations, which aims to approach the inviscid dynamics better than classical dissipation ($\alpha = 1$), for given computational resources. Although its widespread use has been criticized [40], we have made a good case for it in the restricted context of the 2D NSE with periodic boundary conditions in a previous paper [41]. Here, we shall consider only two choices, namely $\alpha = 1$ and $\alpha = 2$.

In the following, $\langle \cdot | \cdot \rangle$ is the classical scalar product in $L^2(\mathbb{T}^2)$, the space of square-integrable functions on \mathbb{T}^2 , $\|\cdot\|$ is the associated norm, and the Fourier transform of a field f on \mathbb{T}^2 is defined by

$$\hat{f}[\mathbf{k}] = \int_{\mathbb{T}^2} f(\mathbf{x}) \exp(-2i\pi \mathbf{k} \cdot \mathbf{x}) d\mathbf{x},$$

where $i = \sqrt{-1}$ and $\mathbf{k} \in \mathbb{Z}^2$. When $\nu = 0$ and when the initial data are smooth, an infinity of integral quantities are preserved by the flow, among which the energy $E = \frac{1}{2} \|\mathbf{u}\|^2$ and the enstrophy $Z = \frac{1}{2} \|\omega\|^2$. When $\nu > 0$, Z decays in time according to

$$\frac{dZ}{dt} + 2\nu P = 0, \quad (2)$$

where $P = \frac{1}{2} \|\nabla \omega\|^2$ is called the palinstrophy.

To use as initial condition we construct a random vorticity field ω_r by letting

$$\hat{\omega}_r[\mathbf{k}] = \begin{cases} \frac{|\mathbf{k}|}{6} e^{i\theta_{\mathbf{k}}} & \text{if } |\mathbf{k}| \leq 6 \\ \left(\frac{|\mathbf{k}|}{6}\right)^{-1} e^{i\theta_{\mathbf{k}}} & \text{if } 6 < |\mathbf{k}| \leq 42 \\ 0 & \text{otherwise,} \end{cases} \quad (3)$$

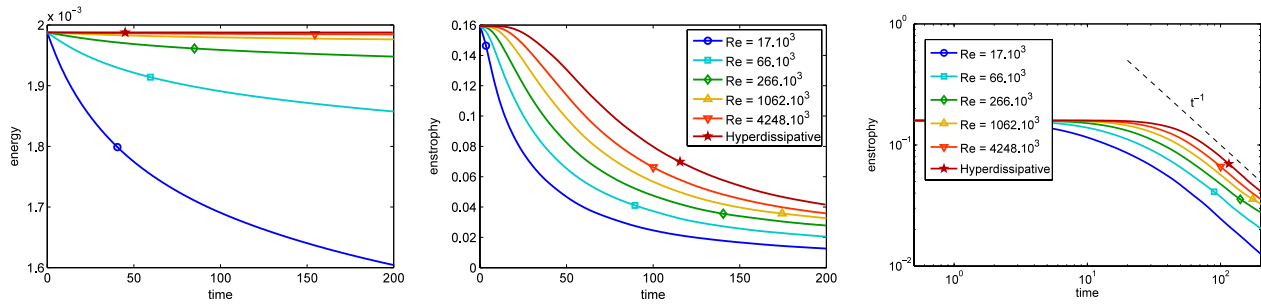


Fig. 1. Time evolution of energy (left) and enstrophy (middle and right) for solutions of the 2D NSE at various Reynolds numbers. The right panel shows the evolution of enstrophy in log–log coordinates along with a t^{-1} reference scaling.

where the θ_k are pseudo-random numbers drawn uniformly in $[0, 2\pi[$. If $E[k]$ denotes the energy spectrum of the flow

$$E[k] = \frac{1}{2} \sum_{k \leq |\mathbf{k}| < k+1} |\hat{\mathbf{u}}[\mathbf{k}]|^2,$$

we have, for ω_r ,

$$E_r[k] \simeq \begin{cases} \frac{\pi k}{36} & \text{if } |k| \leq 6 \\ 36\pi k^{-3} & \text{if } 6 < |k| \leq 42 \\ 0 & \text{otherwise,} \end{cases} \quad (4)$$

which peaks at $k = 6$. Taking ω_r as initial data for the HNSE (1), we shall consider the family of solutions with the parameters mentioned in Table 1 on the time interval $[0, 200]$. Since the initial spectrum slope is compatible with the K67 prediction, a quick development of fine scales is favored, but at the same time dissipative effects do not start to play a role too early. The initial vorticity field is the same for all runs, and only ν and α are varied, so that we approach a single solution to the Euler equations, which is our object of study for the rest of this paper. Its energy is $E_0 = E(0) \simeq 2 \cdot 10^{-3}$ and its enstrophy is $Z_0 = Z(0) \simeq 0.16$. With that the initial eddy turnover time, defined by $\tau = Z(0)^{-1/2}$, is approximately 2.5. Since the initial data is fixed, the only dimensionless parameter playing a role in the NSE is the Reynolds number, which we choose to define by

$$\text{Re} = \frac{Ul}{\nu}, \quad (5)$$

where $l = \frac{1}{6}$ is the integral scale of the initial flow and $U = l^{-1} \sqrt{2E(0)}$ is the initial root mean square (RMS) velocity. When $\alpha > 1$, we do not attempt to define an equivalent Reynolds number.

The HNSE are discretized in space using a classical fully dealiased Fourier pseudo-spectral method, which is equivalent to a Fourier–Galerkin scheme up to round-off accuracy [42]. This ensures that (2) is satisfied by the semi-discrete solution up to round-off accuracy. We denote by K the maximum wavenumber modulus, and the necessary number of grid points in each direction is then $N = 3K$. ν is chosen as small as possible with the constraint that the solution remains well resolved, which in practice means that it should be proportional to $K^{-2\alpha}$ (see Table 1). For time discretization we employ a third-order Runge–Kutta scheme [43, p. 20], together with an integrating factor to accommodate the viscous term. The duration of each timestep is adjusted according to the CFL (Courant, Friedrichs, Lewis [44]) condition. Under these conditions, numerical dissipation due to time-discretization was shown to be negligible in [41]. All computations are made in double precision, and using OpenMP for parallelization.

Table 1

Parameters of reference numerical experiments.

α	1	1	1	1	1	2
$\nu \times 10^7$	6.3	1.6	0.40	0.010	0.0025	8.4×10^{-11}
$\text{Re} \times 10^{-3}$	17	66	266	1062	4248	HNSE
N	512	1024	2048	4096	8192	8192

4. Statistical analysis

4.1. Classical statistics

For consistency with previous work, we check that our solutions behave as expected with respect to classical diagnostics. Energy decays in time with a rate that goes to zero as Re^{-1} (Fig. 1, left), while the enstrophy dissipation rate has an apparent dependency on Re which decays much more slowly when $\text{Re} \rightarrow \infty$ (Fig. 1, middle), in conformity with the results reported by Dmitruk and Montgomery [7] and Tran and Dritschel [8]. The enstrophy decay approaches a t^{-1} behavior for long times (Fig. 1, right), as found by Matthaeus et al. [45]. We note that at $t = 50$ the spectrum has a k^{-3} power law decay range which extends over about two decades (Fig. 2, left), so we consider that a state of fully developed turbulence has been reached. In Fig. 2 (right), we show also for $t = 50$ a histogram of the values taken by the vorticity field on the collocation grid, normalized so that its integral equals 1, which is referred to as a probability distribution function (PDF). The PDFs have an exponential decay for large values of ω , and a relatively flat core region around $\omega = 0$. It is also noteworthy that both the energy spectrum and vorticity PDF appear to converge to a limit when $\text{Re} \rightarrow \infty$, which is consistent with the fact that the solution converges.

4.2. Wavelet transform

In this section, we briefly introduce the wavelet representation, mostly for the sake of notation. Details may be found in textbooks; see, e.g., [46]. Let ψ be a 1-periodic wavelet generating an orthogonal multiresolution analysis of $L^2(\mathbb{T})$, and φ be the associated scaling function. A function f in $L^2(\mathbb{T}^2)$ can be expanded as follows:

$$f = \bar{f} + \sum_{\lambda \in \Lambda} \tilde{f}_\lambda \psi_\lambda, \quad (6)$$

where \bar{f} is the mean value of f on \mathbb{T}^2 , $\tilde{f}_\lambda = \langle f | \psi_\lambda \rangle$,

$$\Lambda = \{\lambda = (j, \mathbf{i}, \mu) \mid j \in \mathbb{N}, \mathbf{i} \in \{0, \dots, 2^j - 1\}^2, \mu \in \{1, 2, 3\}\},$$

and

$$\psi_{(j, \mathbf{i}, 1)}(x_1, x_2) = 2^j \psi(2^j x_1 - i_1) \varphi(2^j x_2 - i_2)$$

$$\psi_{(j, \mathbf{i}, 2)}(x_1, x_2) = 2^j \varphi(2^j x_1 - i_1) \psi(2^j x_2 - i_2)$$

$$\psi_{(j, \mathbf{i}, 3)}(x_1, x_2) = 2^j \psi(2^j x_1 - i_1) \psi(2^j x_2 - i_2).$$

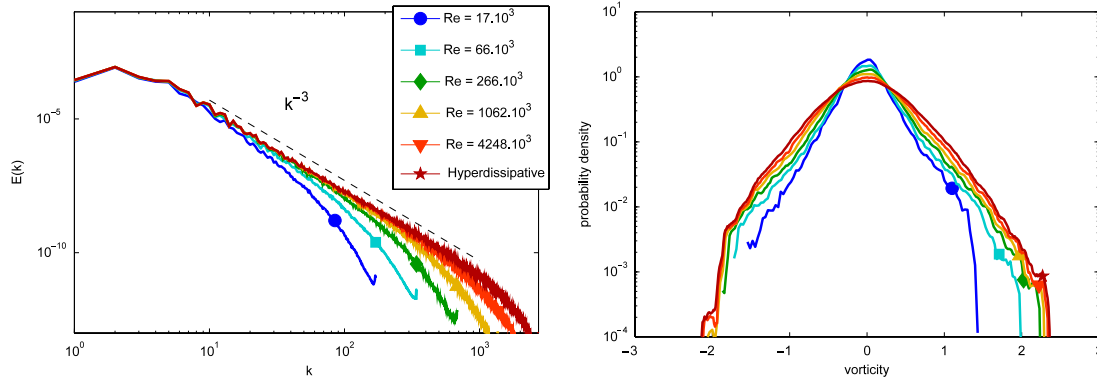


Fig. 2. Energy spectra (left) and vorticity PDFs (right) at $t = 50$ for solutions of the 2D NSE at various Reynolds numbers. Note that the horizontal axis for the PDFs corresponds to the actual vorticity values, and it has not been normalized in any way.

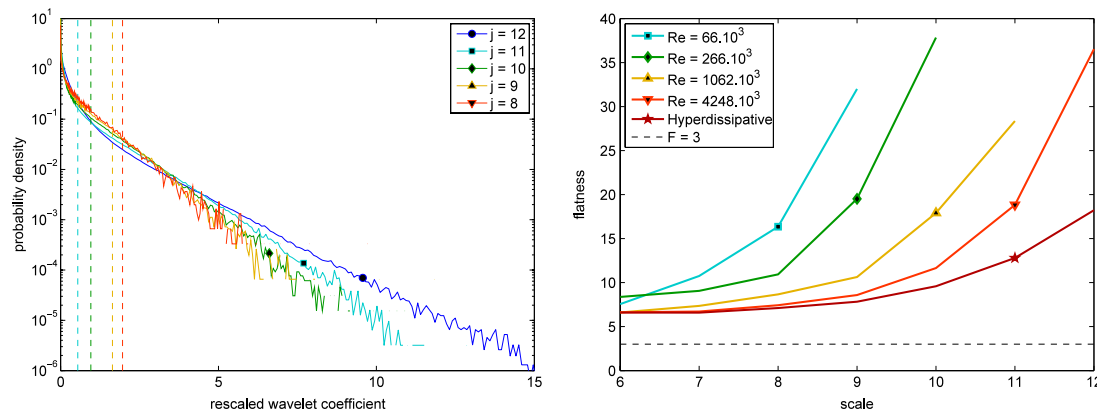


Fig. 3. Left: scale-wise PDFs of vorticity wavelet coefficients for the HNSE reference solution for $t = 50$ and $\mu = 1$. The vertical dashed lines indicate the threshold determined by the scale-wise CVE algorithm; see Section 5.1. Right: scale-wise flatness of vorticity wavelet coefficients for varying Reynolds number for $t = 50$ and $\mu = 1$. The dashed line indicates the value 3, which is the flatness of a Gaussian distribution.

The index j corresponds to the scale of the wavelet, with the conventions that $j = 0$ is the coarsest scale and j increases from coarse to fine scales. The multi-index \mathbf{i} corresponds to the position of the wavelet on the grid of size $2^j \times 2^j$ which is associated to its scale. Finally, the value of μ indicates the directions of oscillation of the wavelet, 1 for the x_1 direction, 2 for the x_2 direction, and 3 for both directions.

In order to approximate the wavelet coefficients of a function using its values at the nodes of a Cartesian grid of size $N \times N = 2^j \times 2^j$, the classical fast wavelet transform algorithm [46] is utilized. The finest scale which is resolved in this manner is $J - 1$. Following earlier work [47], we work with Coiflet wavelets corresponding to filters of length 12 [48].

4.3. Scale-wise statistics

In 3D turbulent flows, energy-containing regions have a smaller and smaller area when going from coarse to fine scales, a phenomenon known as intermittency. To quantify this phenomenon, scale-dependent statistics have often been used, in particular since Sandborn introduced the scale-dependent flatness [49]. Wavelets offer a convenient way of defining scale-dependent statistics and of computing them efficiently. Such statistics have been considered for example in [50] for analyzing fine scale intermittency in anisotropic turbulence. Their relationship with previously introduced statistics that are constructed from structure functions is well known [33]. Their computation for 2D flows instead of 3D flows does not pose any particular technical difficulty, but their behavior, as we recall below, is quite different. In the following, except when otherwise

noted, by scale-dependent statistics we mean quantities that depend on μ and j ; that is, they are also direction dependent.

In an orthogonal wavelet representation, there is no redundancy among the pieces of information corresponding to different scales of the flow, so we may legitimately speak of scale by scale – or *scale-wise* – statistics. The main such object that we would like to focus on is the statistical distribution of the wavelet coefficients of the vorticity field at a given scale and in a given direction. It is a generic scale-wise statistical object, since many others can be recovered from it, for example, all scale-wise moments of the vorticity field. One way of approximating the scale-wise distribution is to consider the PDF of wavelet coefficients within each scale and direction. Surprisingly, such PDFs have not been considered in previous work. They are akin to the well known PDFs of velocity increments [51]. However, the PDFs of velocity increments pose some problems when the spectrum is steeper than k^{-3} [52,53]. Scale-wise PDFs do not suffer from the same shortcoming, provided that the analyzing wavelet has enough vanishing moments [54]. Since we are using a Coiflet with four vanishing moments, we would need to start worrying about seeing the effects of the spectrum of the wavelet itself only if the field we were analyzing had a spectrum steeper than k^{-9} .

The results of the scale-wise analysis for the solutions we have at our disposal are regrouped in Figs. 3 and 4. We focus on $t = 50$ and, since the setup is isotropic, we restrict ourselves to one direction, $\mu = 1$.

We first consider the scale-wise PDF for different scales at the maximum Reynolds number reached by our data (Fig. 3, left). The wavelet coefficients have been rescaled by their standard deviation. All the PDFs have pronounced exponential tails. We notice

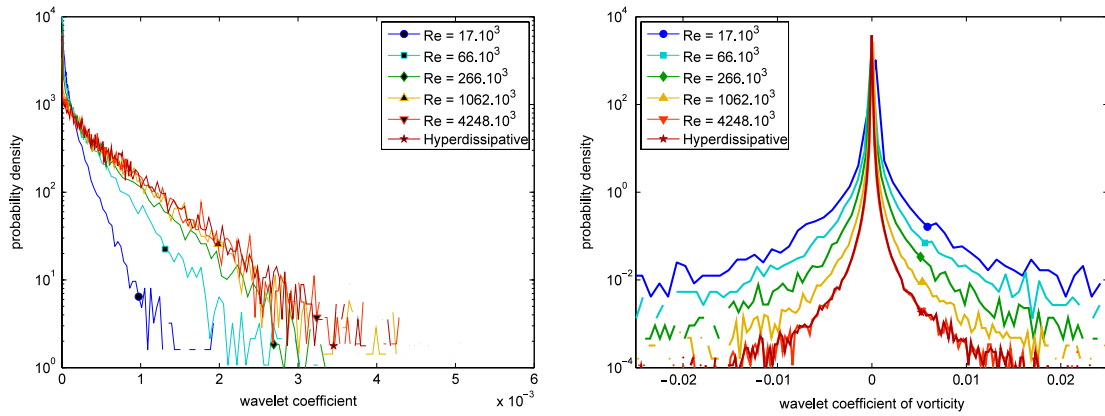


Fig. 4. Wavelet coefficients PDFs in the direction $\mu = 1$ for the reference solutions at $t = 50$, for varying Reynolds number. Left: scale-wise PDF at $j = 7$. Right: global PDF of wavelet coefficients.

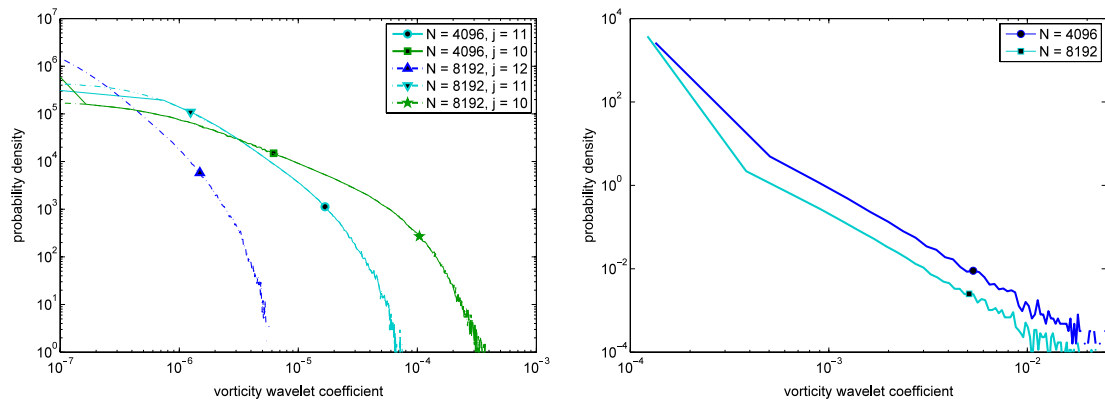


Fig. 5. Comparison of vorticity wavelet coefficient PDFs for the reference flow at $Re \simeq 10^6$ and $t = 50$ (computed with $N = 4096$), and for the same flow upsampled on a grid of size 8192 in each direction. Left: scale-wise PDFs. Right: global PDFs.

that the curves for $j = 8, 9, 10$, corresponding to the inertial range, almost superimpose, while the PDFs corresponding to finer scales $j = 11$ and $j = 12$ have longer tails and a more concave shape. We may therefore conclude that the vorticity field is close to being self-similar in the inertial range of scales, while the behavior in the molecular dissipation range is distinct. This conclusion is supported by the behavior of the scale-wise flatness (Fig. 3, right), which seems to approach a value lying between 6 and 7, independent of scale in the inertial range, as Re increases, while it reaches much higher values in the molecular dissipation range.

We now fix the scale to $j = 7$ and look at the scale-wise PDF of $\tilde{\omega}$ for various Reynolds numbers (Fig. 4, left). We observe convergence towards a limiting curve as Re increases, consistent with our working hypothesis that 2D turbulence has a definite behavior when $Re \rightarrow \infty$. In contrast, the global PDFs of all wavelet coefficients (Fig. 4, right) do not have a limit when $Re \rightarrow \infty$. To understand this, recall that the global PDF can be seen as a mixture of the scale-wise and direction-wise PDFs for all the active scales of motion, each one being weighted by its contribution to the total number of resolved wavelets. Since the finest scale $j = J - 1$ accounts for the majority of wavelet coefficients (75%), and since its behavior is Re dependent, it is not surprising that the global PDF inherits this property.

To push this last point further, one can even consider the global and scale-wise PDFs of the same flow but seen at two different numerical resolutions. In Fig. 5, vorticity wavelet coefficients PDFs are compared for the reference flow computed at $N = 4096$ and $Re \simeq 10^6$, and for the same flow upsampled on a grid with twice the resolution. The upsampling is done in Fourier space, but it more or less boils down to the addition of a new scale $j = 12$ to the

flow with nearly vanishing wavelet coefficients. The changes in the scale-wise PDFs for $j \leq 11$ are too little to be noticed on the graphs, and the curves overlap (Fig. 5, left). In contrast, the change in the global PDF cannot be neglected (Fig. 5, right).

The results that we have presented in this section are consistent with most earlier numerical studies and with experimental studies of flows in soap films, based mostly on structure functions and on vorticity increments statistics; see, for example, the review [55] and references therein. One may summarize the situation by stating that the vorticity statistics are non-Gaussian but nearly self-similar in the inertial range, while intermittency is found in the molecular dissipation range (Fig. 3, left). The main advantage of wavelets over previously used tools is that they form an orthogonal basis: there is no mixing up of information between different scales, and the entire flow can be reconstructed from the wavelet coefficients. The perspectives are appealing, both for computation (see [56]), and for physical modeling, on which we focus in the remaining sections.

Concerning theory, the situation is much less clear. In [9], a correction to the K67 energy spectrum was proposed, which consists in keeping the self-similar k^{-3} range but multiplying it with a logarithmic Re -dependent factor. This stands in contradiction with our numerical results, which indicate that the energy spectrum converges to a Re -independent curve. Moreover, a deviation from exact self-similarity is unavoidable, because the solution converges when $Re \rightarrow \infty$ towards an analytic solution to the Euler equation, which must have an exponentially decaying spectrum for large k . This is a further indication that the important point is not to introduce Re -dependent effects, but, instead, to rethink the way our statistical model is built.

5. Scale-wise coherent vorticity extraction

5.1. Extraction algorithm

The definition of coherent structures in turbulence has been a matter of debate for decades. In [57], it was proposed to define coherent structures as the part of the flow which is not a noise, an approach now known as coherent vorticity extraction (CVE). Such a minimal and negative definition of coherent structures was put forward in the hope that it would be consensual, since it does not rely on the a priori choice of a template for a coherent structure. It also falls neatly in line with the ideas of Kraichnan concerning conditional statistical modeling of turbulence that were reviewed in Section 2. The noise corresponds to information which has been dissipated, while coherent structures correspond to the explicit flow. The price of the approach is that hypotheses need to be made on the noise. As a most simple guess, the noise was assumed to be stationary, additive, Gaussian, and uncorrelated [57], and it was shown that it could be separated from the rest of the vorticity field using wavelet denoising techniques.

The idea behind the denoising algorithm used to single out the coherent part of the vorticity field is as follows. Once ω has been expanded in an orthogonal wavelet basis (Eq. (6)), the terms are split into two groups: coherent terms and incoherent terms. Each coefficient gets attributed to one of the two groups depending on whether its modulus is larger or smaller than a threshold, Θ . An iterative procedure was proposed in [58] in order to find an optimal value of Θ under the assumption that the incoherent part was uncorrelated, which implied in particular that Θ should not depend on scale. We shall refer to such a Θ as a global threshold, and to the associated CVE algorithm as *global CVE*. In previous work, global CVE has been applied to 2D [57,59] and 3D [47,60] turbulence.

In the previous section, we have outlined the fact that the statistics of the wavelet coefficients of a turbulent vorticity field are scale dependent, and shown that over a certain range of scales the scale-wise statistics are resolution independent and have a definite limit when $\text{Re} \rightarrow \infty$, while the global statistics enjoy neither of those two properties. Therefore we would like to propose a modified CVE algorithm, called *scale-wise CVE*, which is based on the idea that the threshold should be scale dependent. In the remaining part of this section, the global CVE and scale-wise CVE algorithms are both thoroughly described. Then, in the remaining sections of the paper, global CVE and scale-wise CVE will be compared from several angles.

For $\Theta > 0$, let $\mathbb{1}_\Theta$ be the indicator function of the interval $[-\Theta, \Theta]$, choose $\lambda = (j, \mathbf{i}, \mu)$, and denote by I_λ the set of all λ' which share with λ the same scale j and the same direction μ . Then define the two quantities:

$$N_\lambda(\Theta) = \sum_{\lambda' \in I_\lambda} \mathbb{1}_\Theta(\tilde{\omega}_{\lambda'}) \quad (7)$$

$$\sigma_\lambda(\Theta)^2 = \frac{1}{N_\lambda(\Theta)} \sum_{\lambda' \in I_\lambda} \mathbb{1}_\Theta(\tilde{\omega}_{\lambda'}) \tilde{\omega}_{\lambda'}^2, \quad (8)$$

which in fact depend only on scale j and direction μ (and not on \mathbf{i}), but for which we keep the multi-index λ for convenience of notation. We remark that $N_\lambda(\Theta)$ is the number of wavelet coefficients at scale j and direction μ that are contained in the interval $[-\Theta, \Theta]$, while $\sigma_\lambda(\Theta)$ is their empirical standard deviation. Then construct by recurrence the sequence $(\Theta_{n,\lambda})_{n \in \mathbb{N}}$ such that

$$\begin{cases} \Theta_{0,\lambda} = \infty \\ \Theta_{n+1,\lambda} = q\sigma_\lambda(\Theta_{n,\lambda}), \end{cases} \quad (9)$$

where q is a dimensionless constant. Iterating forward in the sequence of thresholds $(\Theta_{n,\lambda})_{n \in \mathbb{N}}$ gradually makes the interval $[-\Theta, \Theta]$ tighten around the wavelet coefficients at scale j and direction μ that are close to zero, while expelling those that are far from zero [58]. The latter are known in statistics as “outliers”.

The constant q controls how restrictive our definition of an outlier is. In the following we have taken $q = 2.8$ for scale-wise CVE, so that, for a standard Gaussian random variable, the probability of falling outside the interval $[-q, q]$ is about 0.5%. q can thus be interpreted as a quantile of the standard Gaussian distribution. We should mention that our definition (8) for $\sigma_\lambda(\Theta)$ differs slightly from the one in [58], because we use $N_\lambda(\Theta)$ as the denominator (which is the correct denominator to use when computing a variance), while [58] used the total number of wavelet coefficients. The price of this slight difference is that the proof of convergence of the sequence $(\Theta_{n,\lambda})_{n \in \mathbb{N}}$ given in [58] does not apply to our version of the algorithm. Nevertheless, we observe experimentally that, above a certain value of n (less than 100), $\Theta_{n,\lambda}$ becomes constant with a value Θ_λ satisfying

$$\Theta_\lambda = q\sigma_\lambda(\Theta_\lambda). \quad (10)$$

To increase the compression rate, it was proposed in [59] to use intermediate thresholds belonging to the sequence $(\Theta_{n,\lambda})$ defined by (9), instead of the limit $n \rightarrow \infty$. Different result may be obtained using this technique, but since compression is not our central concern here, we have not considered it. Since the number of distinct wavelet coefficients within scale j and direction μ is 2^{2j} , the very coarse scales of the flow contain too few wavelet coefficients for any statistical quantity to be meaningful, and applying the above procedure to these scales would be quite hazardous. Hence for $j \leq 4$ we prefer to impose $\Theta_\lambda = 0$ (everything is coherent).

Once Θ_λ has been obtained, wavelet coefficients whose modulus lies below Θ_λ , depending on scale j and direction μ , are defined as incoherent, while the remaining ones are defined as coherent. The wavelet coefficients index set Λ is thus split into a set of incoherent coefficients, Λ^I , and a set of coherent coefficients, Λ^C . Note that a similar procedure was independently proposed for data classification in [61]. To impose a regularizing effect of the thresholding operation on the Euler equations [41], we always enforce that $\Theta_\lambda = \infty$ for the finest scale at the current resolution $j = J - 1$. This completes the definition of the scale-wise CVE algorithm.

The global CVE algorithm is obtained if one changes (7)–(8) by extending the sums to all directions and to all scales except the finest one $j = J - 1$, for which we keep $\Theta_\lambda = \infty$, for the reason already mentioned. For global CVE, we have taken $q = 5$, in order to get a compression rate of the same order of magnitude as for scale-wise CVE. In previous publications on global CVE [58–60], the value $q = \sqrt{2 \ln(N^2)}$ (where N is the total number of grid points) was enforced, which is known to be asymptotically optimal for denoising a Gaussian white noise when $N \rightarrow \infty$ [62], but has the disadvantage of being resolution dependent. For comparison, if $N = 2048$, $\sqrt{2 \ln(N^2)} \simeq 5.52$. We shall come back on the touchy issue of the choice of q in the final discussion.

In either case, we then define coherent vorticity ω^C via its wavelet coefficients:

$$\tilde{\omega}_\lambda^C = \mathbb{1}_{\Theta_\lambda}(\tilde{\omega}_\lambda) \tilde{\omega}_\lambda = \begin{cases} \tilde{\omega}_\lambda & \text{if } |\tilde{\omega}_\lambda| \geq \Theta_\lambda \\ 0 & \text{otherwise,} \end{cases} \quad (11)$$

and incoherent vorticity is given by the difference with total vorticity:

$$\omega^I = \omega - \omega^C. \quad (12)$$

Since the wavelet basis is orthogonal, the respective enstrophies Z_C and Z_I of the coherent incoherent part add up to the total enstrophy Z :

$$Z = Z_C + Z_I. \quad (13)$$

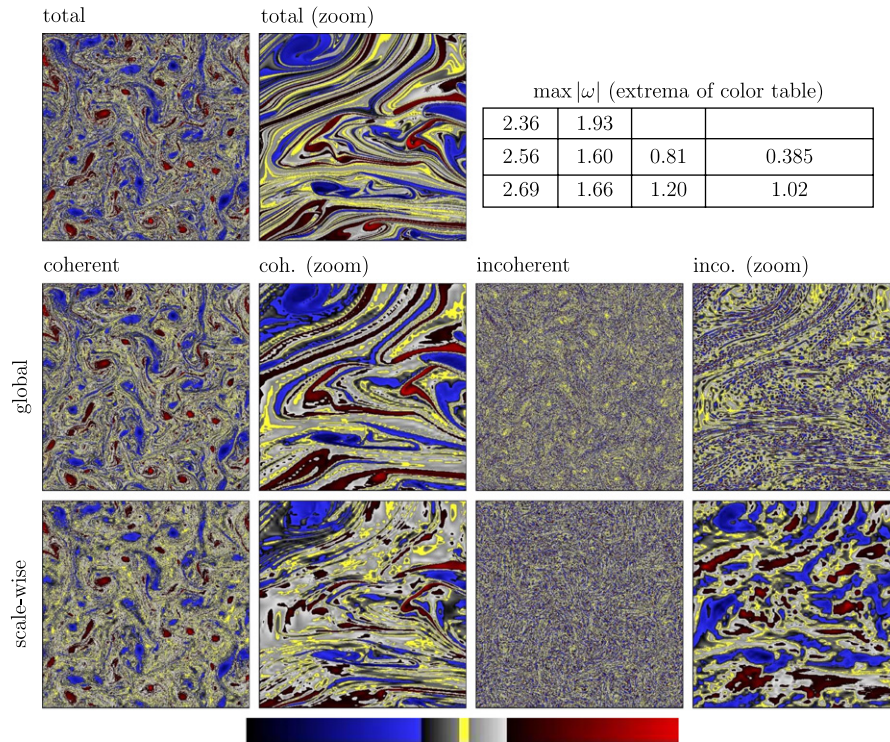


Fig. 6. Snapshots of the total vorticity field (first row), and of its coherent (first and second columns) and incoherent (third and fourth columns) parts for global CVE (middle row) and scale-wise CVE (bottom row). The second (respectively, fourth) column shows a restriction of the coherent (respectively, incoherent) part to the subdomain $[\frac{1}{16}, \frac{1}{16}]$ (corresponding to the lower left corner of the full image). The absolute maxima of the respective fields are given in the table on the top right, following the same arrangement as for the images of the fields. The color table, shown at the bottom of the figure, varies from $-\max|\omega|$ to $+\max|\omega|$ for each picture.

From ω^c and ω^l , coherent and incoherent velocity fields \mathbf{u}^c and \mathbf{u}^l can be reconstructed, but they are in general not orthogonal, so that to define an analogous split for the energy, a cross term needs to be taken into account:

$$E = \frac{1}{2}\|\mathbf{u}^c\|^2 + \frac{1}{2}\|\mathbf{u}^l\|^2 + \langle \mathbf{u}^c | \mathbf{u}^l \rangle = E_c + E_l + E_{cl}. \quad (14)$$

5.2. Results

Now that the global CVE and scale-wise CVE algorithms have been introduced, we apply them to analyze the vorticity fields obtained after the computations described in Section 3, and whose parameters are summarized in Table 1. This section is a follow up on previous results concerning 2D turbulence [57,59], with a strong focus on the two following aspects:

- the dependency on Re in the limit $Re \rightarrow \infty$,
- the interpretation in terms of dissipation.

In Fig. 6, we show snapshots of the vorticity fields obtained by performing the various splits for the HNSE reference solution at $t = 50$. The main structures visible by eye in the total vorticity field are preserved in the coherent vorticity field for both methods (first column). The difference between global CVE and scale-wise CVE is better seen by looking at the incoherent parts (third column): for scale-wise CVE it appears quite homogeneous, whereas for global CVE the remnants of structures can still be glimpsed. Now since the resolution of the field is $N = 8192$ in each direction, its snapshots lack a lot of details, which may give us a false impression. To check this, we look at zooms on small squares of size $\frac{1}{16}$ located in the lower-left corners of each picture (Fig. 6, second and fourth row). Notice that scale-wise CVE enhances most of the sharp features of the vorticity field, while the effect of global CVE is not very pronounced. In fact, as was pointed out already in [59], for global

CVE the coherent part looks very similar to the total vorticity field. In contrast, the distinction is immediate for scale-wise CVE. Perhaps the most striking difference is found on the zooms on the incoherent parts shown in the fourth column: for scale-wise CVE we see a smooth and disorganized field, while for global CVE we see a rough field containing the trace of fine scale filaments.

Now, turning to more quantitative features of the coherent and incoherent flows, we consider their vorticity PDFs (Fig. 7) and energy spectra (Fig. 8, left). For both global CVE and scale-wise CVE, the vorticity PDF is relatively well approximated by the coherent vorticity PDF, and the extrema of the vorticity field are captured by its coherent part. The incoherent vorticity PDFs are supported on a narrower interval and have a nearly Gaussian shape. Quantile–quantile plots (Fig. 7, right) allow us to enhance the deviation with respect to Gaussianness, which is seen to be slightly more pronounced for global CVE than for scale-wise CVE. The distinction between global CVE and scale-wise CVE becomes more evident when looking at the energy spectra (Fig. 8, left). For global CVE, the coherent energy spectrum closely follows the total energy spectrum except in the molecular dissipation range, where incoherent energy becomes dominant, in agreement with earlier results [59]. However, the k^{-1} scaling of the incoherent energy spectrum (corresponding to enstrophy equipartition) that was observed in [59] is confirmed here only over a restricted range of wavenumbers, while the overall shape of the incoherent energy spectrum seems better described by a k^0 scaling. For scale-wise CVE, the total, coherent, and incoherent energy spectra all have a k^{-3} scaling range. The incoherent spectrum falls down more rapidly than the coherent one in the far inertial range, and therefore the coherent part becomes dominant in the dissipative range, while in the inertial range coherent and incoherent enstrophies are of the same order of magnitude. Recall that for scale-wise CVE all wavelet coefficients at scales $j \leq 4$ are automatically coherent. Therefore the behavior of the

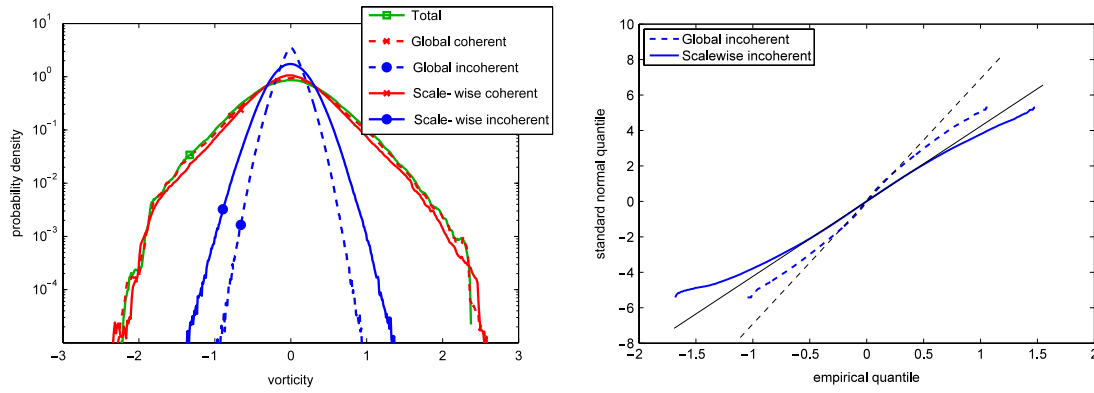


Fig. 7. Analysis of total, coherent, and incoherent flows, as defined by scale-wise CVE (full lines) and global CVE (dashed lines), for the HNSE reference solution at $t = 50$. Left: vorticity PDFs. Right: quantile–quantile plots of the incoherent vorticities versus the standard normal distribution. Linear fits corresponding to normal distributions with matching means and standard deviations are shown for comparison.

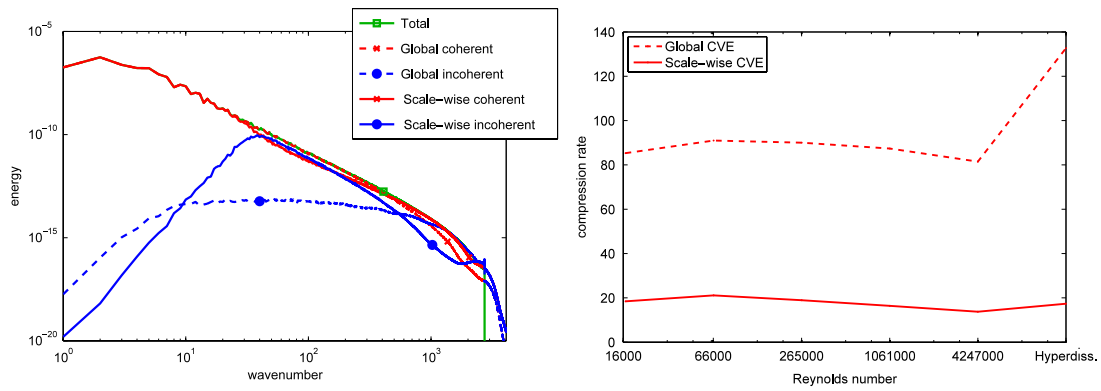


Fig. 8. Left: energy spectra of total, coherent, and incoherent flows, as defined by scale-wise CVE (full lines) and global CVE (dashed lines), for the HNSE reference solution at $t = 50$. Right: compression rate as a function of Reynolds number for global CVE and scale-wise CVE.

incoherent spectrum for $k \leq 16$ is just a byproduct of the spectrum of the analyzing wavelet.

Since one of our goals is to compare the potential benefits of global CVE and scale-wise CVE for the design of adaptive numerical schemes, it is also important to measure how much the amount of information contained in the flow is reduced if one keeps track explicitly only of coherent vorticity instead of total vorticity. The measurement of information is a difficult problem, which we shall come back to in Section 7.1. Here, we limit ourselves to a well known diagnostic, the compression rate \mathcal{R} , defined by

$$\mathcal{R} = \frac{\#\Lambda}{\#\Lambda_c},$$

where $\#\cdot$ denotes the number of elements in a set. \mathcal{R} is plotted as a function of Reynolds number in Fig. 8 (right). We observe that \mathcal{R} is close to 20 for scale-wise CVE and close to 80 for global CVE. The higher value, close to 130, reached for global CVE with hyperdissipation can be explained by the fact that global CVE is more sensitive to the behavior of the wavelet coefficients in the dissipation range, which is quite different for the hyperdissipative solution, as can be deduced from its scale-wise flatness (Fig. 3, right). Overall, an improvement in the compression rate when Re increases is observed neither for global CVE nor for scale-wise CVE. Further study will be necessary to determine if this result also applies to wall-bounded 2D turbulence or to 3D turbulence (see [63,60] for recent results along this line).

Based on the above results, we would like to conjecture that, for scale-wise CVE, in the limit $\text{Re} \rightarrow \infty$, the incoherent enstrophy and energy both converge to a nonzero limit. To test this conjecture, consider the energy and enstrophy of the flow at $t = 50$,

normalized by their initial values, as functions of Reynolds number (Fig. 9). In agreement with the literature [7,8], the molecular enstrophy dissipation vanishes as $\text{Re} \rightarrow \infty$, so the ratio $\frac{Z(t=50)}{Z(t=0)}$ approaches 1. For global CVE, the amount of incoherent enstrophy is small and nearly Re independent, while, for scale-wise CVE, it increases with Re. Unfortunately, a saturation regime for incoherent enstrophy is not reached in the range of Re that we have been able to consider. However, such a regime is reached for incoherent energy (Fig. 9, right), albeit at a relatively low fraction of about 2×10^{-3} of the initial energy. Hence the conjecture is valid at least for energy, and is likely to be valid also for enstrophy. For global CVE, incoherent energy goes to zero as Re^{-1} . Since the main difference between the HNSE and the NSE solutions is the behavior in the dissipation range, the fact that the last points stand out on the curves corresponding to global CVE suggests that the latter is most sensitive to this range of scales, a property that we have already encountered earlier.

Now that we have established the statistical properties of the coherent and incoherent parts, we would like to assess the practical relevance of the split as regards the 2D Euler dynamics. As a first step in that direction, we consider the enstrophy transfers, both between the coherent and incoherent parts, and between different scales of motion.

6. Interscale enstrophy transfers and production of incoherent enstrophy

6.1. Transfers in Fourier space

In the regime that we are considering, enstrophy is transferred on average from low wavenumber modes to large wavenumber

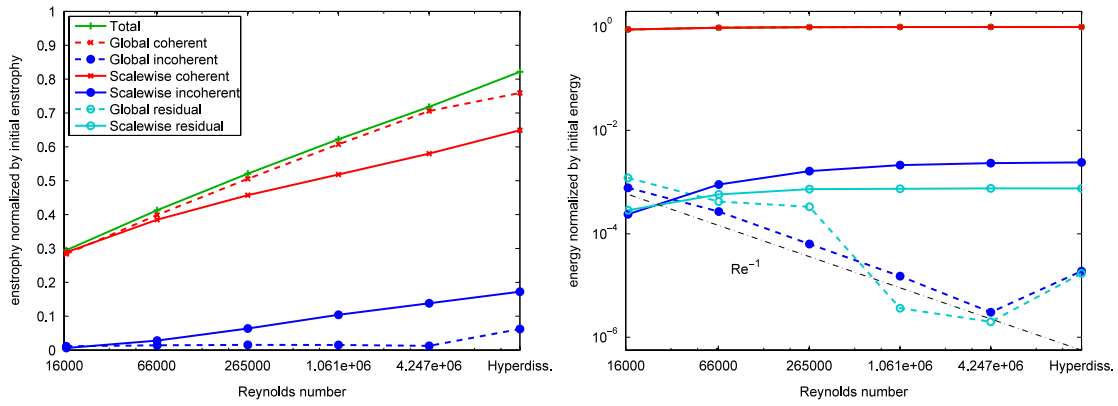


Fig. 9. Euler invariants of total, coherent, and incoherent flows, as defined by scale-wise CVE (full lines) and global CVE (dashed lines), at $t = 50$, as functions of Reynolds number. Left: enstrophy, normalized by the initial enstrophy $Z(0)$. Right: energy, normalized by the initial energy $E(0)$, and plotted with a logarithmic vertical scale.

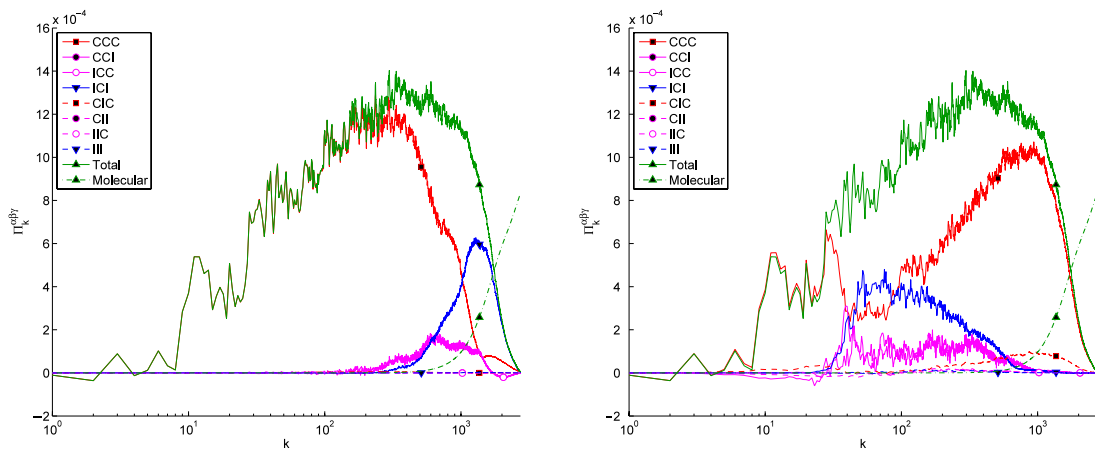


Fig. 10. Contributions to enstrophy transfer between Fourier modes. Left: global CVE. Right: scale-wise CVE.

modes. To quantify this process, it is convenient to introduce the orthogonal projector P_k on modes with wavenumbers whose modulus is smaller than k :

$$P_k(f) = \sum_{|\mathbf{k}| \leq k} \hat{f}[\mathbf{k}] \exp(2i\pi \mathbf{k} \cdot \mathbf{x}),$$

and the vorticity field can then be split as follows:

$$\omega = P_k \omega + (1 - P_k) \omega,$$

where the two terms are orthogonal to each other. Thanks to the Pythagoras identity, the enstrophy can in turn be split into two terms: $Z = Z_{\leq} + Z_{>} = \frac{1}{2} \|P_k \omega\|^2 + \frac{1}{2} \|(1 - P_k) \omega\|^2$, and the goal is to determine the transfer from Z_{\leq} to $Z_{>}$, or the interscale enstrophy transfer.

The procedure is classic (see, e.g., [1]) but we would like to recall it in detail here since it will serve as an introduction to the next paragraph where wavelet transfers are to be considered. One first writes down the evolution equation for Z_{\leq} by bracketing the NSE with $P_k(\omega)$:

$$\frac{dZ_{\leq}}{dt} + \langle \mathbf{u} \cdot \nabla \omega | P_k \omega \rangle + \nu \langle \Delta \omega | P_k \omega \rangle = 0. \quad (15)$$

Then one may define a trilinear form a by

$$a(\omega_1, \mathbf{u}, \omega_2) = \langle \mathbf{u} \cdot \nabla \omega_1 | \omega_2 \rangle, \quad (16)$$

where \mathbf{u} is a divergence-free vector field, and ω_1, ω_2 are scalar fields. The essential property of a is that it is antisymmetric with respect to its first and last variables [64]: $a(\omega_1, \mathbf{u}, \omega_2) =$

$-a(\omega_2, \mathbf{u}, \omega_1)$, and in particular for any \mathbf{u} and ω_1 we have $a(\omega_1, \mathbf{u}, \omega_1) = 0$. Using that property along with (15), one finally obtains the system

$$\begin{cases} \frac{dZ_{\leq}}{dt} + a((1 - P_k)\omega, \mathbf{u}, P_k \omega) + \nu \|\nabla P_k \omega\|^2 = 0 \\ \frac{dZ_{>}}{dt} - a((1 - P_k)\omega, \mathbf{u}, P_k \omega) + \nu \|(1 - P_k)\omega\|^2 = 0, \end{cases} \quad (17)$$

where Z_{\leq} and $Z_{>}$ are now ostensibly coupled by the transfer term

$$\Pi_k = a((1 - P_k)\omega, \mathbf{u}, P_k \omega). \quad (18)$$

Following [60], we would like to discriminate between the coherent and incoherent contributions to Π_k . Since Π_k is trilinear, eight such contributions can be pulled out:

$$\Pi_k^{\alpha\beta\gamma} = a((1 - P_k)\omega^\alpha, \mathbf{u}^\beta, P_k \omega^\gamma), \quad (19)$$

where $(\alpha, \beta, \gamma) \in \{I, C\}^3$. To make the distinction with the next section clear, let us insist on the fact that, for any choice of α, β and γ , $\Pi_k^{\alpha\beta\gamma}$ is just part of the transfer from Z_{\leq} to $Z_{>}$, but contains no information about the production of incoherent enstrophy.

$\Pi_k^{\alpha\beta\gamma}$ is plotted as a function of k in Fig. 10, for the HNSE reference simulation at $t = 50$. For global CVE (Fig. 10, left), we find that the term Π_{CCC} dominates the transfers in the inertial range, while some other terms become non negligible only in the molecular dissipation range. This is not surprising, given what we have learned in the previous section, namely that the fraction of incoherent enstrophy is very low in the inertial range.

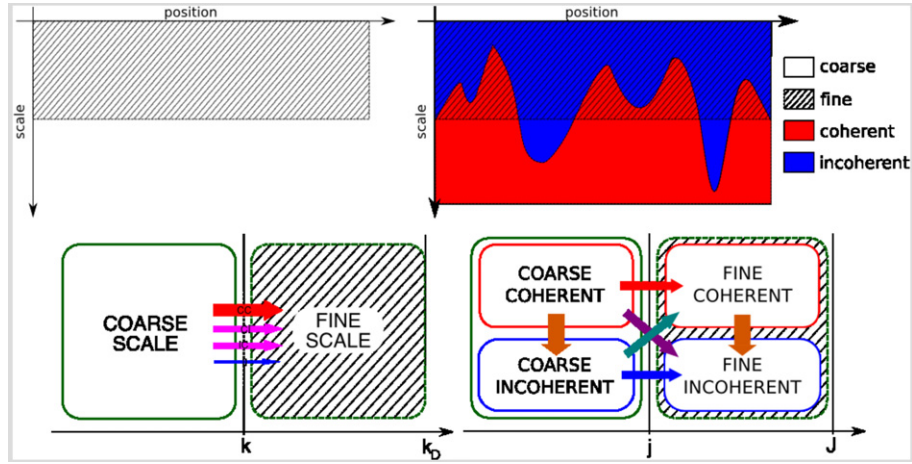


Fig. 11. Top row: schematic view of the segmentation used in the wavelet transfer analysis (Section 6.2). On the left, only the distinction between coarse and fine scales is made, while on the right coherent and incoherent coefficients are considered separately. Bottom row: diagram showing the possible enstrophy transfer paths. Left: transfers in Fourier space. Right: transfers in wavelet space.

The four transfer terms associated to the incoherent velocity field, namely $\Pi^{al\gamma}$ (Fig. 10, dashed lines), are two to three orders of magnitude smaller than those associated to the coherent velocity field (Fig. 10, full lines). For scale-wise CVE, all terms of type $\Pi^{\alpha C\gamma}$ are non-negligible throughout the inertial range, which means that both the coherent and incoherent parts participate in the nonlinear transfer of enstrophy from low wavenumber modes to large wavenumber modes. The term Π^{ClC} also participates to the transfer with a share of up to 10%.

6.2. Transfers in wavelet space

The above procedure may be followed again, but this time starting from an orthogonal wavelet basis instead of the Fourier basis [32]. The projector P_k is replaced by \tilde{P}_j , the orthogonal projector on the subspace generated by wavelets whose scale is coarser than j . One ends up with a wavelet interscale transfer term $\tilde{\Pi}_j$ which is the exact analog of Π_k defined by (18). Two main disadvantages have to be put up with when considering transfers in wavelet space as opposed to Fourier space.

- In addition to the effect of the nonlinear term, there can be an enstrophy transfer due to the molecular dissipation term. Indeed, the nice decoupling observed in (17) was possible because the projector P_k commutes with the Laplace operator, whereas \tilde{P}_j does not.
- The wavelets are not as localized in Fourier space as the Fourier modes themselves. This is a price to pay for the space localization of the wavelets.

The bright side is that wavelets allow us to refine the transfer analysis by looking separately at the coherent and incoherent parts, as we now proceed to explain. Let us assume that the set Λ^C of coherent wavelet coefficients is chosen by applying one of the two algorithms of the previous section, either global CVE, or scale-wise CVE. There are three types of contribution to the enstrophy transfers between the coherent and the incoherent parts:

- the coupling by the nonlinear term,
- the coupling by the molecular dissipation term,
- the change in time of the sets Λ^C and Λ^I .

Here we shall leave out the second contribution, since we are mostly interested in nonlinear transfers, and also the third contribution, by assuming that Λ^C and Λ^I are fixed.

Denoting by \tilde{P}^C the projector on wavelets ψ_λ such that $\lambda \in \Lambda^C$, and $\tilde{P}^I = 1 - \tilde{P}^C$, we may thus split the enstrophy as follows:

$$Z = \frac{1}{2} \|\tilde{P}^C \tilde{P}_j \omega\|^2 + \frac{1}{2} \|\tilde{P}^I \tilde{P}_j \omega\|^2 \quad (20)$$

$$+ \frac{1}{2} \|\tilde{P}^C (1 - \tilde{P}_j) \omega\|^2 + \frac{1}{2} \|\tilde{P}^I (1 - \tilde{P}_j) \omega\|^2 \quad (21)$$

$$= Z_{\leq}^C + Z_{\leq}^I + Z_{>}^C + Z_{>}^I. \quad (22)$$

Given that \tilde{P}^C and \tilde{P}_j commute and are both orthogonal, a system of four equations similar to (17) can be derived to describe the time evolution of the four terms. The difference between the Fourier and wavelet viewpoints is summarized by the diagram in Fig. 11. A similar kind of diagram was introduced in [65] to describe the stochastic coherent adaptive large eddy simulation (SCALES) computational approach. However, the enstrophy transfers between the various components have not been measured before.

The wavelet transfers are shown in Fig. 12, for the HNSE reference solution at $t = 50$. While reading the following discussion, keep in mind that we are analyzing a single realization at a single instant, and that we are not making any stationarity hypothesis. We are not attempting to extract scaling laws, but rather we are focusing on understanding CVE in relation to the time-dependent Navier–Stokes dynamics.

The total enstrophy transfer from coarse to fine scales ($\leq \rightarrow >$) is in agreement with the result obtained in the previous section using Fourier analysis. So is the molecular dissipation effect. Key differences between global CVE and scale-wise CVE are revealed by looking at the other curves. For global CVE (Fig. 12, left), the production of incoherent enstrophy ($C_{\leq} \rightarrow I_{\leq}$ and $C_{\leq} \rightarrow I_{>}$) occurs only at scales where molecular dissipation cannot be neglected. At coarser scales, all the enstrophy transfers are dominated by $C_{\leq} \rightarrow C_{>}$, that is, the transfer of coherent enstrophy from coarse to fine scales, similarly to what was observed for energy in 3D turbulence [60].

Since in the case of scale-wise CVE the dependency with j is quite complex, let us first consider a single abscissa, $j = 9$. The transfers, expressed as percentages of the total nonlinear transfer, are shown in Table 2. The situation as a result of global CVE is also shown for comparison purposes. The first important thing that we notice is that for scale-wise CVE, and contrary to global CVE, the production of incoherent enstrophy ($C_{\leq} \rightarrow I_{\leq}$) is of the same order of magnitude as the interscale transfer $C_{\leq} \rightarrow C_{>}$. Recall the

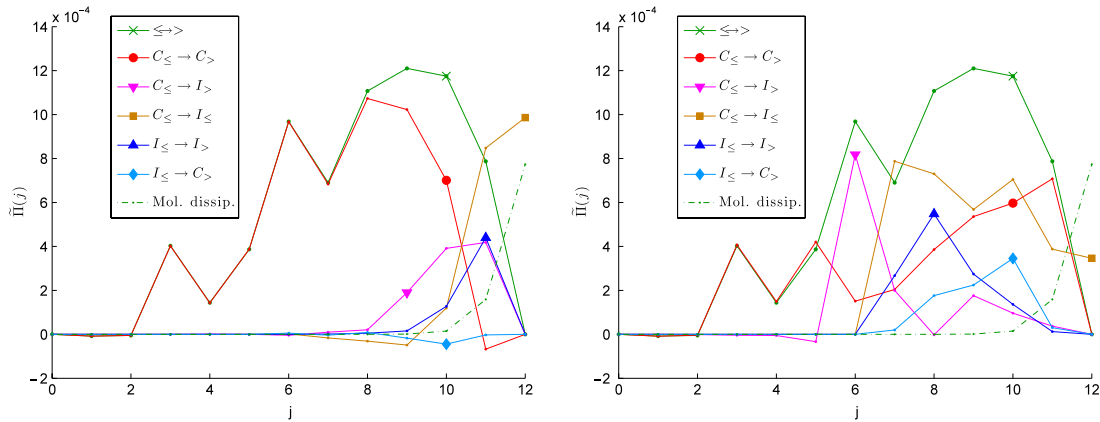


Fig. 12. Wavelet transfers. Top: global CVE. Bottom: scale-wise CVE.

Table 2

Wavelet enstrophy transfers across $j = 9$ for global CVE and scale-wise CVE applied to the reference HNSE solution at $t = 50$. The numbers are expressed as percentages relative to the total interscale transfer ($\le \rightarrow >$).

	Global (%)	Scale-wise (%)
$C_{\le} \rightarrow C_{>}$	92.3	48.4
$C_{\le} \rightarrow I_{>}$	17.1	15.9
$C_{>} \rightarrow I_{\le}$	-1.58	-20.2
$I_{\le} \rightarrow I_{>}$	1.39	24.8
$\le \rightarrow >$	100	100
$C_{\le} \rightarrow I_{\le}$	-4.4	51.3

comment of Kraichnan [20]: the processes which mix enstrophy at scales $j \leq 9$ act on the same time scale as the processes which send enstrophy from C_{\le} to $C_{>}$. Next, we should mention the transfer $C_{>} \rightarrow I_{\le}$, which measures how much of the fine scale coherent enstrophy is transferred to coarse scale incoherent enstrophy. From the point of view that we have adopted, any transfer $C \rightarrow I$ is seen as a dissipation of enstrophy. Hence the fact that the transfer $C_{>} \rightarrow I_{\le}$ is negative and non-negligible (-23%) raises the issue of *negative dissipation*. Notice that the same property holds for global CVE, albeit with a smaller amplitude. But we should not be scandalized by observing negative dissipation in turbulent flows. Indeed, it is well known that organized structures do spontaneously emerge out of initially random flows. The CVE approach has the merit of quantifying this phenomenon.

Now let us turn to Fig. 12 (right), which shows the j -dependency of the transfers in the case of scale-wise CVE. We consider only scales $j \geq 5$, since below $j = 4$ everything was assumed to be coherent in the definition of the algorithm. The first thing to note is that for $6 \leq j \leq 9$ the dependency of the transfers on j is relatively benign, and the various terms keep the same orders of magnitude. We thus recover the almost self-similar behavior that could be deduced from the scale-wise statistics. But looking more closely, it appears that the transfer due to the coherent part tends to increase when going to finer scales. We interpret this as a time-dependent effect: the initial condition consists only of coarse scale motion, and it takes some time for incoherent enstrophy to build up and to start transferring energy to fine scales. The behavior for $j \geq 10$ is also worthy of some notice, especially since it is highly counterintuitive. Indeed, when molecular dissipation dominates, one may expect the transfers to be mostly incoherent, as was the case for global CVE. But the situation is quite the opposite: for $j = 10$ and $j = 11$, the transfer is actually dominated by the $C_{\le} \rightarrow C_{>}$ term.

We now come back to the overall picture, as it may be understood from the wavelet transfer analysis. It appears that global CVE behaves in a manner which is similar to molecular dissipation: indeed, the production of incoherent part occurs mostly in the dissipative range of scales, while the nonlinear

transfer in the inertial range is associated almost exclusively to the coherent part. Scale-wise CVE offers a more radical view point on the inertial range in 2D turbulence, by splitting the interscale transfer of enstrophy into two parallel channels, one associated to the coherent part, and one associated to the incoherent part. The enstrophy transfers through both channels are of the same order of magnitude, although only a few percent of the wavelet coefficients of the coherent vorticity field are nonzero. Since the scale-wise PDFs do not depend much on j in the inertial range, there is a small fraction of coherent coefficients within each scale. From the two previous sentences we may infer that the transfer of enstrophy through the coherent channel is due to localized events, involving few wavelet coefficients, while the transfer through the incoherent channel is much more homogeneous in space. The dominant exchange between the two channels is the conversion of coherent into incoherent enstrophy, $C_{\le} \rightarrow I_{\le}$, but there is also a non-negligible backwards conversion $I_{\le} \rightarrow C_{>}$, which is maximal in the far inertial range, i.e., just before the dissipation range. This negative dissipation feeds the fine scale coherent part, and may act as a source of flow intermittency in the dissipation range [66]. As a result, in the dissipation range, the flow is intermittent, and the dominant channel is the coherent one.

From the above discussion, we conjecture that simulation using global CVE does not need a turbulence model, and can thus be considered as DNS (see also [41]). In contrast, a turbulence model would be necessary for simulation based on scale-wise CVE in order to take into account the retroaction of the incoherent part onto the coherent part. This will be the topic of the next section.

7. Dynamical influence of the incoherent part

7.1. Randomization as dissipation

As pointed out in the introduction, it is said that a quantity is dissipated when the corresponding degrees of freedom are replaced by random variables. The remaining explicitly computed degrees of freedom are then perturbed stochastically by the dissipated (e.g., incoherent) ones. We would like to find out more about this perturbation in the two specific cases of global CVE and scale-wise CVE.

When a wavelet coefficient indexed by λ is replaced by a random variable, we say that it has been randomized, and we denote it W_{λ} . We have already defined in Section 5.1 the index set of incoherent wavelet coefficients according to global CVE and to scale-wise CVE. There remains to choose a probability distribution for the random vector $(W_{\lambda})_{\lambda \in \mathcal{A}'}$. A natural constraint that we would like to impose is that applying the randomization operator twice in a row is equivalent to applying it only once, that is, that

the operator is idempotent. For this condition to hold exactly, the incoherent coefficients must stay below the threshold

$$\tilde{W}_\lambda \in [-\theta_\lambda, \theta_\lambda], \tag{23}$$

and the value of the threshold itself should stay invariant under randomization, implying that

$$\mathbb{E}(\tilde{W}_\lambda) = 0, \tag{24}$$

and also, because of Eq. (10),

$$\frac{1}{N_\lambda(\theta_\lambda)} \sum_{\lambda' \in \Lambda^l \cap \lambda} \tilde{W}_{\lambda'}^2 = \left(\frac{\theta_\lambda}{q}\right)^2. \tag{25a}$$

Under these three constraints, the most unbiased choice that we may make is the distribution which maximizes the Shannon entropy, that is, the uniform distribution on the manifold defined by Eqs. (23) and (25a) in $\mathbb{R}^{\#\Lambda^l}$, that is, the intersection of a hypersphere and of a hypercube. Unfortunately, we have not found an efficient way of generating pseudo-random numbers distributed accordingly. Hence, for practical reasons, we propose to replace (25a) with the more tractable constraint that

$$\mathbb{E}(\tilde{W}_\lambda^2) = \left(\frac{\theta_\lambda}{q}\right)^2, \tag{25b}$$

which ensures that enstrophy is conserved by the randomization operator in the ensemble average sense. Note the analogy of (25a) with the conservation of internal energy characterizing the microcanonical ensemble, and of (25b) with the temperature constraint of the canonical ensemble.

We admit that the solution of the entropy maximization problem under the three constraints ((23)–(24)–(25b)) can be factorized into a product of univariate distributions f_λ . To maximize the entropy of f_λ it is convenient to first rescale it by its standard deviation:

$$f_\lambda(w) = \frac{1}{\sigma_\lambda} f_0\left(\frac{w}{\sigma_\lambda}\right),$$

and then solve the equivalent problem of maximizing the entropy of the rescaled distribution

$$S(f_0) = \int_{\mathbb{R}} f_0 \ln(f_0)$$

under the constraints that f_0 has variance 1 and is supported on $[-q, q]$. The solution turns out to be a truncated Gaussian distribution, given by

$$f_0(w) = \begin{cases} \mathcal{Z} \exp\left(-\frac{w^2}{2s_0^2}\right) & \text{if } |w| \leq q \\ 0 & \text{otherwise,} \end{cases}$$

where \mathcal{Z} is a normalization factor and the value of s_0 has to be chosen so that

$$\int_{-q}^q dw w^2 f_0(w) = \frac{\int_{-q}^q w^2 \exp\left(-\frac{w^2}{2s_0^2}\right) dw}{\int_{-q}^q \exp\left(-\frac{w^2}{2s_0^2}\right) dw} = 1, \tag{26}$$

which is imposed by Eq. (10). s_0 can be understood as a dilation factor which compensates for the truncation of the wings of the Gaussian distribution by slightly dilating it in order to preserve its variance. Provided that $q > \sqrt{3}$, (26) admits a unique real solution which we approximate using a numerical solver. The entropy of f_λ is then

$$S(f_\lambda) = S(f_0) + \ln(\sigma_\lambda), \tag{27}$$

and the total entropy S of the flow is then by definition the entropy of the tensor product of the f_λ for $\lambda \in \Lambda^l$, which is simply obtained from (27) by summation. In this framework, the increase

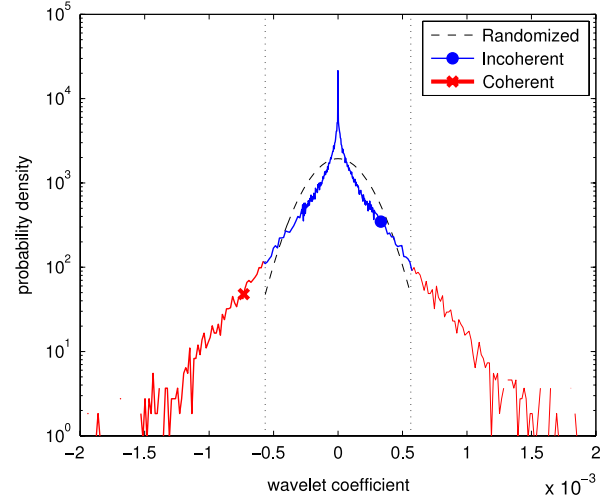


Fig. 13. For the HNSE reference solution at $t = 50$, comparison between the empirical PDFs of the coherent and incoherent vorticity wavelet coefficients at scale $j = 8$ (full red (curve with a cross) and blue (curve with a full circle) lines) and the analytical PDF (Eq. (26)) obtained after maximizing the entropy (black dashed line). The vertical dotted lines indicate the interval $[-\theta, \theta]$, where θ is the threshold.

Table 3

The four dissipation mechanisms considered in Section 7.

Type of CVE	Fate of incoherent part	Shorthand
Global	Discarded	GD
Global	Randomized	GR
Scale-wise	Discarded	SD
Scale-wise	Randomized	SR

of incoherent enstrophy at a given scale implies an increase of entropy, which is consistent with our interpretation in terms of dissipation.

In Fig. 13, the truncated Gaussian PDF resulting from entropy maximization is shown alongside the empirical PDF of vorticity wavelet coefficients at scale $j = 8$ and for $t = 50$, as obtained from the HNSE reference solution. Notice that the truncated Gaussian PDF does not approach the empirical PDF well, since it is much less peaked around zero.

7.2. Method

We would like to find out what the consequences of the loss of information implied by the statistical model that we have just built are regarding our ability to predict the explicit flow. To do this we adopt a Monte Carlo approach. We start from the NSE reference solution at $t = 50$ for $N = 2048$ and $Re \simeq 2.66 \cdot 10^5$. Ten different realizations of the randomization operators are applied to the vorticity field, and the NSE are then integrated separately up to $t = 100$ for each one of them. In practice, normally distributed random numbers with standard deviation s_λ are generated using the Mersenne twister algorithm, and the \tilde{W}_λ are obtained by retaining only those that fall within the interval $[-\theta_\lambda, \theta_\lambda]$. For comparison, we also consider the case where the incoherent part is completely discarded instead of being randomized. The four cases that we are going to compare are summarized in Table 3. There remains to decide under what terms the comparison is to be performed.

Defining a meaningful way of comparing several turbulent flows is a research topic in itself, closely connected to the chosen statistical framework. In the setting of complete statistical modeling, only quantities characterizing the attractor of the dynamical system corresponding to the turbulent flow may be meaningfully compared, since all other properties are considered to be random.

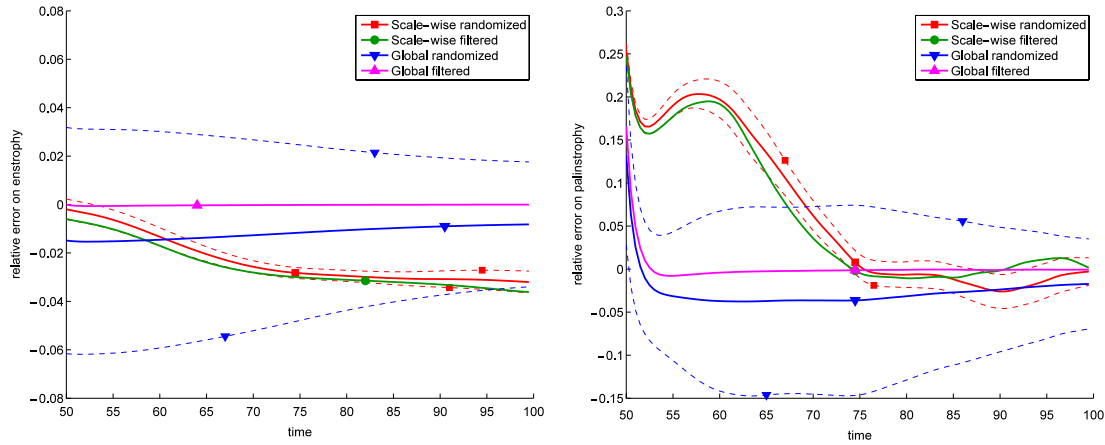


Fig. 14. Relative error on integral quantities as a function of time between the filtered and randomized flows and the reference flow at $N = 2048$. The error is averaged over ten realizations of the randomization operator. The dashed lines are one standard deviation away from the average. Left: enstrophy. Right: palinstrophy.

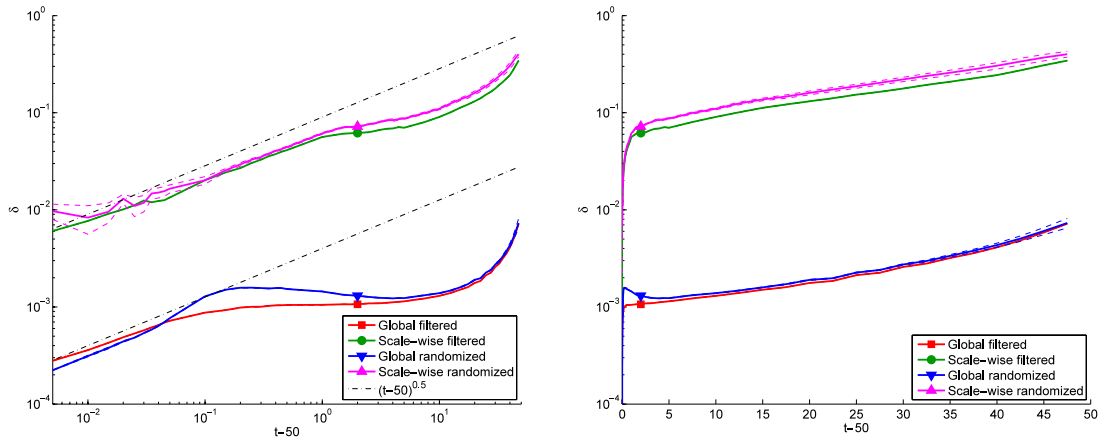


Fig. 15. Left: time evolution of the average error between the reference and perturbed solutions, as defined by Eq. (28), on log–log scales. The dashed lines delimit an interval of one standard deviation above and below the average error, as can be estimated from ten realizations. The dashed–dotted lines indicate the scaling $\delta(t) \propto (t - t_0)^{\frac{1}{2}}$. Right: same data, but represented using a linear scale for the horizontal axis.

In contrast, in a completely deterministic framework, one wishes to compare two solutions of the Navier–Stokes equations point-wise in space and in time, but that may yield little relevant information since the dynamics are known to be chaotic, i.e., unstable to perturbations. Two solutions initially very close to each other will always end up far away, even though it is not yet completely clear what influences the rate of separation. As an intermediate between these two extreme approaches, we propose to compare only the explicit flows, as defined within the framework of the conditional statistical model we are working with.

Even within a given statistical framework, there remains the question of what features of the flow are to be compared. On the one hand, we shall consider integral quantities, namely enstrophy and palinstrophy, which we know to be predictable because they have been stabilized by spatial averaging. But it is also important to assess to what extent local properties of the flow can be predicted as well. Therefore, we shall consider the measure

$$\delta_X(t) = \frac{\|\mathbf{u}_X^C(t) - \mathbf{u}^C(t)\|}{\|\mathbf{u}^C(t)\|}, \quad (28)$$

where X stands for either one of the four dissipation mechanisms recalled in Table 3, $\mathbf{u}_X^C(t)$ is the coherent velocity field of the perturbed solution at time t , and $\mathbf{u}^C(t)$ is the coherent velocity field of the reference solution at time t .

Table 4

Initial value of δ_X for the four dissipation mechanisms, averaged over ten realizations.

X	GD	GR	SD	SR
$\langle \delta_X(0) \rangle$	1.5×10^{-21}	2.5×10^{-13}	1.1×10^{-19}	2.5×10^{-7}

7.3. Results

We observe that the enstrophy of the randomized flow (Fig. 14, left) decays on average faster than the one of the reference flow, while remaining close to it. The palinstrophy (Fig. 14, right) gets on average larger for the randomized vorticity field at $t = 50$, but comes back to the reference value after $t = 75$. For enstrophy, at $t = 50$, the fluctuation level among the ensemble of randomized solutions is a few percent, and for palinstrophy it is goes up to 25%.

Let us now turn to the evolution in time of the difference between the perturbed and reference solutions, as defined by Eq. (28). As expected, the initial values of δ are close to the round-off precision for SD and GD (Table 4). They are also quite small for SR and GR, thanks to the constraints imposed on the randomization algorithm as described in the previous section. To lower $\delta(0)$ for SR and GR even more, we would need a microcanonical randomization operator, which we have not achieved in the present work. The evolution in time of δ (Fig. 15) goes through two

distinct phases, which are the same for the four operators:

1. a power-law behavior for short times, which can be roughly described by the scaling $\delta(t) \propto (t - 50)^{\frac{1}{2}}$, and
2. an exponential growth for large times.

The ratio between the errors for global CVE and for scale-wise CVE keeps the same order of magnitude 10^{-2} , independent of time. Although scale-wise CVE initially attributes a larger proportion of the energy and enstrophy to the dissipated flow than global CVE, and thereby entails a bigger loss of information, the dissipated flows associated to global and to scale-wise CVE retroact on the explicit flow in proportion to their initial amplitude, and can be seen as equivalent in this respect. The singularity of $\delta(t)$ in $t = 0$ is also a property common to both approaches, and is probably linked to the lack of regularity of their respective thresholding operators.

8. Conclusion

In this paper, we have undertaken an extensive statistical analysis of 2D turbulence in the enstrophy cascade regime, by numerical study of solutions of the Navier–Stokes equations in the vanishing viscosity limit, and using the wavelet representation of the vorticity field as the essential mathematical tool. We have shown that the classical enstrophy cascade phenomenology could be recovered in the wavelet representation, by considering the scale-wise statistics, and interscale enstrophy transfers. By computing the scale-wise PDFs of the wavelet coefficients, we have been able to extract more information than is contained in the more classical energy spectrum and structure functions. From a practical point of view, wavelet statistics are appealing because they can be obtained efficiently without computing the Fourier transform of the vorticity field, and can be generalized to non-periodic boundary conditions and adaptive grids. Another advantage which may become more and more important is the scaling efficiency of the parallel wavelet transform, which is in theory better than the one of the parallel Fourier transform.

We have introduced scale-wise coherent vorticity extraction (CVE) as a way to separate extreme events and very probable events within each scale of the flow. Formally a simple extension of the existing global CVE approach, scale-wise CVE has the advantages of being much more robust in the limit $Re \rightarrow \infty$, and of being independent of numerical discretization effects. Scale-wise CVE yields an incoherent part which contains a non negligible fraction of the total enstrophy of the flow, and also a small fraction of the energy. There are good indications that both fractions may converge to a nonzero limit when $Re \rightarrow \infty$. We propose that the productions of incoherent vorticity and energy are Re -independent measures of dissipation for 2D turbulence. This dissipation should be understood in a “subjective” sense [24], as a transfer of enstrophy between degrees of freedom that we choose to compute explicitly and degrees of freedom that we choose to model statistically. Yet once it has been defined, this dissipation can be quantified in a fully rigorous way by considering the transfers between various regions of wavelet space, as we have done in Section 6.2. We have shown that, contrary to global CVE, for which the intrascale transfer of enstrophy in the inertial range is dominated by its coherent component, scale-wise CVE entails a non-negligible intrascale transfer of incoherent enstrophy in the inertial range.

These findings shed a new light on earlier results that have shown how the 2D and 3D Navier–Stokes [59,60] and 2D Euler [41] dynamics were well preserved by discarding after each timestep the incoherent part determined from global CVE. Our explanation is that global CVE acts mostly in the dissipation range, and does not influence the inertial range. Thanks to its nonlinear character, global CVE may stand as a more judicious choice than a classical, linear dissipation operator, since it allows for a more economical

representation of the flow in the dissipation range by greatly reducing the number of necessary degrees of freedom. As a counterpart, we expect the compression rate that can be attained by global CVE to be limited by the size of the dissipation range. For example, taking the three finest scales as a rough estimate of the dissipation range in a standard, well resolved turbulent flow, the compression rate for global CVE can not increase much above 64 in 2D and 512 in 3D. Anyway, for 2D homogeneous turbulence, we have shown here that neither global CVE nor scale-wise CVE induces the pronounced increase of the compression rate with Re that would be necessary to make the approach computationally competitive. We expect that the situation will be different for 3D flows, or even for 2D flows with boundaries, which we propose to study in detail in future work.

Turbulent dissipation entails a loss of information which affects our ability to predict the explicit flow exactly. To estimate the error on the explicit flow, we have introduced a statistical model for the dissipated flow. We have first defined an ensemble of flows endowed with a probability measure obtained by maximizing the entropy under minimal realistic constraints. The elements of this ensemble are all the realizations of the total flow that are compatible with the observed explicit flow, or in other words they are conditioned by the explicit flow. Adopting a Monte Carlo approach, we have picked from this ensemble ten different perturbations of the reference flow, and we have integrated them in time. By monitoring the time evolution of enstrophy and palinstrophy, we have checked that the global properties of the ten flow realizations are close to those of the reference solution. This finding is not very surprising, since integral quantities such as enstrophy and palinstrophy are generally thought to be quite stable to perturbations. To benefit from a more discriminating test, we have then considered the time evolution of the error between the perturbed and reference solutions. To measure the error, we have projected both the perturbed and reference solutions using the same filter as the one used to generate the perturbation. We have shown that the L^2 error on the coherent flow velocity first undergoes a power-law growth, with an exponent close to 0.5, and then a relatively slow exponential growth. The explicit flow is thus sufficient to partially predict the time evolution of the total flow for more than ten eddy turnover times, both for global CVE and scale-wise CVE. The performance is especially good for global CVE, for which the relative L^2 error remains below 1% on that same period.

An important limitation of the present work is that our splitting algorithms, both global CVE and scale-wise CVE, depend on the choice of a constant q (see Eq. (9)). We have not studied the dependency of our results on this constant, and we have not been able to provide a rigorous justification for the choice of q . We conjecture that q can be used as a control parameter to enhance or degrade the faithfulness of the representation of the flow by its coherent part. This remains an important subject for future research. More generally, one should define an objective way of deciding when a split is better than another split, although the choice of how accurate one wants the final results to be is likely to remain subjective.

An interesting perspective is to implement the split that we have proposed as a turbulence model in a numerical code. Much work has already been done on adaptive codes in wavelet bases [59,67,56], and the novelty would be to include the stochastic terms modeling the incoherent part. Our randomization technique could also benefit ensemble forecasting, whose performance depends heavily on the way the ensemble of initial conditions is constructed.

Acknowledgments

The authors would like to thank Claude Bardos, Mathias Holschneider, Rupert Klein, and Edriss Titi for inspiring discussions, and Greg Hammett for an important remark concerning

wavelet filtering. The three authors thank the Wissenschaftskolleg zu Berlin for its hospitality, as well as the SMAI and the organizers of CEMRACS 2010 for supporting their stay at CIRM (Marseille, France) while writing this paper, and IDRIS-CNRS for providing computing time. We acknowledge financial support from the Euratom–CEA Association, the French Federation for Fusion Studies, and the PEPS program of CNRS-INSMI.

Legal notice

This work, supported by the European Communities under the contract of Association between EURATOM, CEA and the French Research Federation for Fusion Studies, was carried out within the framework of the European Fusion Development Agreement. The views and opinions expressed herein do not necessarily reflect those of the European Commission.

References

- [1] R.H. Kraichnan, Inertial ranges in two-dimensional turbulence, *Phys. Fluids* 10 (1967) 1417–1423.
- [2] G.K. Batchelor, Computation of the energy spectrum in homogeneous two-dimensional turbulence, *Phys. Fluids* 12 (1969) (II)233–(II)239.
- [3] J.R. Chasnov, On the decay of two-dimensional homogeneous turbulence, *Phys. Fluids* 9 (1997) 171–180.
- [4] K.K. Golovkin, Vanishing viscosity in the Cauchy problem for the equations of hydromechanics, *Trudy Mat. Inst. Steklov* 92 (1966) 31–49.
- [5] A. Pouquet, M. Lesieur, J.C. André, C. Basdevant, Evolution of high Reynolds number two-dimensional turbulence, *J. Fluid Mech.* 72 (1975) 305–319.
- [6] G.K. Vallis, Remarks on the predictability properties of two- and three-dimensional flow, *Quart. J. Roy. Meteor. Soc.* 111 (1985) 1039–1047.
- [7] P. Dmitruk, D.C. Montgomery, Numerical study of the decay of enstrophy in a two-dimensional Navier–Stokes fluid in the limit of very small viscosities, *Phys. Fluids* 17 (2005) 035114.
- [8] C.V. Tran, D.G. Dritschel, Vanishing enstrophy dissipation in two-dimensional Navier–Stokes turbulence in the inviscid limit, *J. Fluid Mech.* 559 (2006) 107–116.
- [9] D.G. Dritschel, C.V. Tran, R.K. Scott, Revisiting Batchelor’s theory of two-dimensional turbulence, *J. Fluid Mech.* 591 (2007) 379–391.
- [10] P.A. Davidson, Cascades and fluxes in two-dimensional turbulence, *Phys. Fluids* 20 (2008) 025106.
- [11] C. Bardos, E. Titi, Euler equations for incompressible ideal fluids, *Russian Math. Surveys* 62 (2007) 409–451.
- [12] J. Pedlosky, *Geophysical Fluid Dynamics*, Springer, 1987.
- [13] J.M. Burgers, On the resistance experienced by a fluid in turbulent motion, *Proc. KNAW* 26 (1923) 582–604.
- [14] G.I. Taylor, Statistical theory of turbulence, *Proc. R. Soc. London, Ser. A* 151 (1935) 421–444.
- [15] C. Basdevant, R. Sadourny, Ergodic properties of inviscid truncated models of two-dimensional incompressible flows, *J. Fluid Mech.* 69 (1975) 673–688.
- [16] D. Ruelle, F. Takens, On the nature of turbulence, *Commun. Math. Phys.* 20 (1971) 167–192.
- [17] P. Bradshaw, Turbulence: the chief outstanding difficulty of our subject, *Exp. Fluids* 16 (1994) 203–216.
- [18] J. Bricmont, Science of chaos or chaos in science? in: P.R. Gross, N. Levitt, M.W. Lewis (Eds.), in: *The Flight from Science and Reason*, vol. 775, The New York Academy of Sciences, 1996, pp. 131–175.
- [19] R. Balian, *From Microphysics to Macrophysics*, Springer, 2006.
- [20] R.H. Kraichnan, On Kolmogorov’s inertial-range theories, *J. Fluid Mech.* 62 (1974) 305–330.
- [21] R.H. Kraichnan, S. Chen, Is there a statistical mechanics of turbulence? *Physica D* 37 (1989) 160–172.
- [22] R.H. Kraichnan, Irreversible statistical mechanics of incompressible hydro-magnetic turbulence, *Phys. Rev.* 109 (1958) 1407–1422.
- [23] R.H. Kraichnan, Reduced descriptions of hydrodynamic turbulence, *J. Stat. Phys.* 51 (1988) 949–963.
- [24] L.F. Richardson, J.A. Gaunt, Diffusion regarded as a compensation for smoothing, *Mem. R. Meteorol. Soc.* 3 (1930) 171–175.
- [25] L. Prandtl, Über die ausgebildete Turbulenz, *Z. Ang. Math. Mech.* 5 (1925) 136–139.
- [26] J.W. Deardorff, A numerical study of three-dimensional turbulent channel flow at large Reynolds numbers, *J. Fluid Mech.* 41 (1970) 453–480.
- [27] T. Dubois, F. Jauberteau, R. Temam, Solution of the incompressible Navier–Stokes equations by the nonlinear Galerkin method, *J. Sci. Comput.* 8 (1993) 167–194.
- [28] R.S. Ellis, K. Haven, B. Turkington, Large deviation principles and complete equivalence and nonequivalence results for pure and mixed ensembles, *J. Stat. Phys.* 101 (2000) 999–1064.
- [29] B. Turkington, A. Majda, K. Haven, M. Dibattista, Statistical equilibrium predictions of jets and spots on Jupiter, *Proc. Natl. Acad. Sci. USA* 98 (2001) 12346–12350.
- [30] A. Eisner, B. Turkington, Nonequilibrium statistical behavior of nonlinear Schrödinger equations, *Physica D* 213 (2006) 85–97.
- [31] M. Farge, G. Rabreau, Transformée en ondelettes pour détecter et analyser les structures cohérentes dans les écoulements turbulents bidimensionnels, *C. R. Acad. Sci. Paris Série II* b 307 (1988) 433–440.
- [32] C. Meneveau, Dual spectra and mixed energy cascade of turbulence in the wavelet representation, *Phys. Rev. Lett.* 66 (1991) 1450–1453.
- [33] M. Farge, E. Goirand, Y. Meyer, F. Pascal, M.V. Wickerhauser, Improved predictability of two-dimensional turbulent flows using wavelet packet compression, *Fluid Dyn. Res.* 10 (1992) 229–250.
- [34] E.T. Jaynes, Where do we go from here? in: C. Ray Smith, W.T. Grandy (Eds.), *Maximum-Entropy and Bayesian Methods in Inverse Problems*, D. Reidel Publishing Company, 1985.
- [35] C.E. Shannon, A mathematical theory of communication, *Bell Labs Tech. J.* 27 (1948) 379–423, 623–656.
- [36] E.T. Jaynes, Information theory and statistical mechanics, *Phys. Rev.* 106 (620–630) (1957) 171–190, 108.
- [37] C. Meneveau, J. Katz, Scale-invariance and turbulence models for large-eddy simulation, *Ann. Rev. Fluid Mech.* 32 (2000) 1–32.
- [38] O.A. Ladyzhenskaya, *The Mathematical Theory of Viscous Incompressible Flow*, Gordon and Breach, 1963.
- [39] C. Basdevant, B. Legras, R. Sadourny, M. Bédard, A study of barotropic model flows: intermittency, waves and predictability, *J. Atmospheric Sci.* 38 (1981) 2305–2326.
- [40] U. Frisch, S. Kurien, R. Pandit, W. Pauls, S. Sankar Ray, A. Wirth, J.-Z. Zhu, Hyperviscosity, Galerkin truncation and bottlenecks in turbulence, *Phys. Rev. Lett.* 101 (2008) 144501.
- [41] R. Nguyen van yen, M. Farge, K. Schneider, Wavelet regularization of a Fourier–Galerkin method for solving the 2D incompressible Euler equations, *ESAIM: Proc.* 29 (2009) 89–107.
- [42] C. Canuto, A. Quarteroni, M.Y. Hussaini, T.A. Zang, *Spectral Methods in Fluid Dynamics*, Springer-Verlag, 1988.
- [43] P. Orlandi, *Fluid Flow Phenomena: A Numerical Toolkit*, Springer, 2000.
- [44] R. Courant, K. Friedrichs, H. Lewy, Über die partiellen Differenzgleichungen der mathematischen Physik, *Math. Ann.* 100 (1) (1928) 32–74.
- [45] W.H. Matthaeus, W.T. Stribling, D. Martinez, S. Oughton, D. Montgomery, Selective decay and coherent vortices in two-dimensional incompressible turbulence, *Phys. Rev. Lett.* 66 (1991) 2731–2734.
- [46] S. Mallat, *A Wavelet Tour of Signal Processing*, Academic Press, 1999.
- [47] M. Farge, G. Pellegrino, K. Schneider, Coherent vortex extraction in 3D turbulent flows using orthogonal wavelets, *Phys. Rev. Lett.* 87 (2001) 054501.
- [48] I. Daubechies, Orthormal bases of compactly supported wavelets II. Variations on a theme, *J. Math. Anal.* 24 (1993) 499–519.
- [49] V.A. Sandborn, Measurements of intermittency of turbulent motion in a boundary layer, *J. Fluid Mech.* 6 (1959) 221–240.
- [50] W.J.T. Bos, L. Liechtenstein, K. Schneider, Small-scale intermittency in anisotropic turbulence, *Phys. Rev. E* 76 (2007) 046310.
- [51] P. Kailasnath, K.R. Sreenivasan, G. Stolovitzky, Probability density of velocity increments in turbulent flows, *Phys. Rev. Lett.* 68 (1992) 2766–2769.
- [52] A. Babiano, C. Basdevant, R. Sadourny, Structure functions and dispersion laws in two-dimensional turbulence, *J. Atmospheric Sci.* 42 (1985) 941–949.
- [53] L. Biferale, M. Cencini, A.S. Lanotte, D. Vergni, Inverse velocity statistics in two-dimensional turbulence, *Phys. Fluids* 15 (2003) 1012–1020.
- [54] K. Schneider, M. Farge, N. Kevlahan, Spatial intermittency in two-dimensional turbulence: a wavelet approach, in: N. Tongring, R. Penner (Eds.), in: *Perspectives in Mathematics and Physics*, vol. 34, World Scientific, 2004, pp. 302–328.
- [55] P. Tabeling, Two-dimensional turbulence: a physicist approach, *Phys. Rep.* 362 (2002) 1–62.
- [56] K. Schneider, O. Vasilyev, Wavelet methods in computational fluid dynamics, *Annu. Rev. Fluid Mech.* 42 (2010) 473–503.
- [57] M. Farge, K. Schneider, N. Kevlahan, Non-Gaussianity and coherent vortex simulation for two-dimensional turbulence using an adaptive orthogonal wavelet basis, *Phys. Fluids* 11 (1999) 2187–2201.
- [58] A. Azzalini, M. Farge, K. Schneider, Nonlinear wavelet thresholding: a recursive method to determine the optimal denoising threshold, *Appl. Comput. Harmon. Anal.* 18 (2004) 177–185.
- [59] K. Schneider, M. Farge, A. Azzalini, J. Zuber, Coherent vortex extraction and simulation of 2D isotropic turbulence, *J. Turbulence* 7 (2006) N44.
- [60] N. Okamoto, K. Yoshimatsu, K. Schneider, M. Farge, Y. Kaneda, Coherent vortices in high resolution direct numerical simulation of homogeneous isotropic turbulence: a wavelet viewpoint, *Phys. Fluids* 19 (2007) 115109.
- [61] C. Hennig, Clusters, outliers, and regression: fixed point clusters, *J. Multivariate Anal.* 86 (2003) 183–212.
- [62] D. Donoho, I. Johnstone, Ideal spatial adaptation by wavelet shrinkage, *Biometrika* 81 (1994) 425–455.
- [63] N. Kevlahan, J. Alam, O.V. Vasilyev, Scaling of space time modes with Reynolds number in two-dimensional turbulence, *J. Fluid Mech.* 570 (2007) 217–226.
- [64] C. Foiaš, O. Manley, R. Rosa, R. Temam, *Navier–Stokes Equations and Turbulence*, CUP, 2001.
- [65] D.E. Goldstein, O.V. Vasilyev, Stochastic coherent adaptive large eddy simulation method, *Phys. Fluids* 16 (2004) 2497–2513.
- [66] M. Farge, M. Holschneider, T. Philipovitch, Formation et stabilité des structures cohérentes quasi-singulières en turbulence bidimensionnelle, *C. R. Acad. Sci. Paris, series II* 315 (1992) 1585–1592.
- [67] G. Keetels, U. D’Ortona, W. Kramer, H. Clercx, K. Schneider, G.J. van Heijst, Fourier spectral and wavelet solvers for the incompressible Navier–Stokes equations with volume-penalization: convergence of a dipole–wall collision, *J. Comput. Phys.* 227 (2007) 919–945.